AI-Based Discovery and CryoEM Structural Elucidation of a K_{ATP} Channel Pharmacochaperone

Assmaa ElSheikh[1,2], Camden M. Driggers[1], Ha H. Truong[3], Zhongying Yang[1], John Allen[1], Niel Henriksen[3], Katarzyna Walczewska-Szewc[4], and Show-Ling Shyng[1*]

[1]Department of Chemical Physiology and Biochemistry, Oregon Health & Science University, Portland, OR 97239, USA; [2] Department of Medical Biochemistry, College of Medicine, Tanta University, Tanta, Egypt; [3]Atomwise Inc., 250 Sutter St., Suite 650, San Francisco, CA, USA; [4]Institute of Physics, Faculty of Physics, Astronomy and Informatics, Nicolaus Copernicus University in Toruń, ul. Grudziądzka 5, 87-100 Toruń, Poland.

*To whom correspondence may be addressed: Show-Ling Shyng (ORCID: 0000-0002-8230-8820), Department of Chemical Physiology and Biochemistry, School of Medicine, Oregon Health & Science University, 3181 S.W. Sam Jackson Park Road, Portland, OR 97239, email:shyngs@ohsu.edu.

Key words: ATP-sensitive potassium channel, cryoEM structure, Kir6.2, SUR1, ABC transporter, pharmacological chaperones, drug discovery

Abbreviations: K_{ATP}, ATP-sensitive potassium channel; Pharmacochaperone, pharmacological chaperone; CHI, congenital hyperinsulinism; cryoEM, cryo-electron microscopy; AI, artificial intelligence; Kir6.2, inward-rectifying potassium channel 6.2; SUR1, sulfonylurea receptor 1; ATP, adenosine triphosphate; ADP, adenosine diphosphate; GBC, glibenclamide; RPG, repaglinide; CBZ, carbamazepine; ABC protein, ATP-binding cassette protein; NBD, nucleotide binding domain of SUR1; TM, transmembrane; TMD, transmembrane domain; ER, endoplasmic reticulum; KNtp, Kir6.2 N-terminal peptide; GPCR, G-protein coupled receptor; CFTR, cystic fibrosis transmembrane conductance regulator protein.

Abstract

Pancreatic K_{ATP} channel trafficking defects underlie congenital hyperinsulinism (CHI) cases unresponsive to the K_{ATP} channel opener diazoxide, the mainstay medical therapy for CHI. Current clinically used K_{ATP} channel inhibitors have been shown to act as pharmacochaperones and restore surface expression of trafficking mutants; however, their therapeutic utility for K_{ATP} trafficking impaired CHI is hindered by high-affinity binding, which limits functional recovery of rescued channels. Recent structural studies of K_{ATP} channels employing cryo-electron microscopy (cryoEM) have revealed a promiscuous pocket where several known K_{ATP} pharmacochaperones bind. The structural knowledge provides a framework for discovering K_{ATP} channel pharmacochaperones with desired reversible inhibitory effects to permit functional recovery of rescued channels. Using an AI-based virtual screening technology AtomNet® followed by functional validation, we identified a novel compound, termed Aekatperone, which exhibits chaperoning effects on K_{ATP} channel trafficking mutations. Aekatperone reversibly inhibits K_{ATP} channel activity with a half-maximal inhibitory concentration (IC_{50}) ~ 9 μM. Mutant channels rescued to the cell surface by Aekatperone showed functional recovery upon washout of the compound. CryoEM structure of K_{ATP} bound to Aekatperone revealed distinct binding features compared to known high affinity inhibitor pharmacochaperones. Our findings unveil a K_{ATP} pharmacochaperone enabling functional recovery of rescued channels as a promising therapeutic for CHI caused by K_{ATP} trafficking defects.

Introduction

Pancreatic β-cells secret insulin in response to an increase in blood glucose levels to maintain glucose homeostasis. Central to this process is the ATP-sensitive potassium (K_{ATP}) channel assembled from four pore-forming Kir6.2 subunits (encoded by *KCNJ11*) and four regulatory SUR1 subunits (encoded by *ABCC8)* (Aguilar-Bryan & Bryan, 1999; Ashcroft, 2023; Driggers & Shyng, 2023; Nichols, 2006*)*. K_{ATP} channels are gated by intracellular ATP and ADP, the concentrations of which change following glucose metabolism. This enables K_{ATP} channels to couple blood glucose levels with β-cell membrane potential to control insulin secretion (Ashcroft, 2023; Merrins et al., 2022; Nichols et al., 2022; Thompson & Satin, 2021). When serum blood glucose levels rise, the intracellular ATP/ADP ratio increases, which promotes K_{ATP} channel closure, membrane depolarization, Ca^{2+} influx through voltage-gated Ca^{2+} channels, and insulin secretion. Conversely, a fall in serum glucose reduces the intracellular ATP/ADP ratio, which favors opening of K_{ATP} channels, leading to membrane hyperpolarization and termination of insulin secretion. Underscoring the importance of β-cell K_{ATP} channels in glucose regulation, gain of function K_{ATP} mutations cause neonatal diabetes, while loss of function K_{ATP} mutations cause congenital hyperinsulinism (CHI) (Ashcroft, 2023; De Franco et al., 2020; ElSheikh & Shyng, 2023; Nichols et al., 2022; Pipatpolkai et al., 2020). K_{ATP} inhibitors such as sulfonylureas and glinides or activators such as diazoxide may be used to treat diseases caused by gain or loss of function K_{ATP} mutations respectively; however, effectiveness of these existing drugs is highly dependent on the underlying mutant channel defects (ElSheikh & Shyng, 2023; Martin et al., 2020; Pipatpolkai et al., 2020; Rosenfeld et al., 2019). A case in point is congenital hyperinsulinism caused by mutations in *ABCC8* or *KCNJ11* that prevent proper folding and assembly of the channel proteins in the endoplasmic reticulum (ER) and subsequent trafficking of K_{ATP} channels to the β-cell plasma membrane (Cartier et al., 2001; Crane & Aguilar-Bryan, 2004; ElSheikh & Shyng, 2023; Fukuda et al., 2011; Yan et al., 2004; Yan et al., 2007). Individuals harboring such mutations present severe CHI disease unresponsive to diazoxide and often require pancreatectomy to prevent life-threatening hypoglycemia. For these patients, drugs that overcome K_{ATP} channel trafficking defects are needed (ElSheikh & Shyng, 2023).

Pharmacological chaperones (pharmacochaperones) are small molecules that bind to target proteins and facilitate their folding, assembly, and trafficking (Bernier et al., 2004; Convertino et al., 2016; Leidenheimer & Ryder, 2014). Previous work has shown that K_{ATP} channel inhibitors act as pharmacochaperones to overcome K_{ATP} trafficking defects (Martin et al., 2020). Among these inhibitor pharmacochaperones, glibenclamide (GBC), a high affinity sulfonylurea, and repaglinide (RPG), a high affinity glinide, have long been used clinically for type 2 diabetes (Sahin et al., 2024); in addition, carbamazepine (CBZ), an anti-convulsant known to inhibit voltage-gated Na^+ channel, has been found to potently inhibit K_{ATP} channels (Chen et al., 2013; Devaraneni et al., 2015; Martin et al., 2016; Yan et al., 2004; Yan et al., 2006). Kir6.2 is a transmembrane (TM) protein with two TM helices and cytoplasmic N- and C-termini. SUR1, a member of the ABC protein family, consists of a canonical ABC core structure of two 6-TM helix TM domains (TMD), TMD1 and TMD2, and two cytoplasmic nucleotide binding domains (NBDs), NBD1 and NBD2; in addition, it contains an N-terminal TM domain TMD0 which is connected to the ABC core via a cytoplasmic linker, L0 (Driggers & Shyng, 2023). Recent high resolution cryoEM structures of K_{ATP} channels along with functional studies revealed that K_{ATP} inhibitors bind at a common pocket in the transmembrane domain of the SUR1-ABC core that serves to anchor and immobilize the Kir6.2 N-terminus, which interaction stabilizes nascent channel assembly and hence trafficking to the cell surface (Martin, Kandasamy, et al., 2017; Martin et al., 2020; Martin et al., 2019; Martin, Yoshioka, et al., 2017). Paradoxically, the same SUR1-Kir6.2 interaction also results in channel closure, explaining the dual pharmacochaperone

and inhibitory effects of the aforementioned compounds. Thus, a current challenge in harnessing the pharmacochaperone effects of the above known K_{ATP} inhibitors to treat CHI caused by K_{ATP} trafficking mutations is their relatively high binding affinity, which impedes channel functional recovery post-rescue (ElSheikh & Shyng, 2023). Inhibitor pharmacochaperones with lower affinity for K_{ATP} channels would allow their rapid dissociation from rescued channels at the cell surface upon pharmacochaperone washout for channel function.

K_{ATP} channel drug discovery to date has historically involved serendipitous findings, modification of existing scaffolds with medicinal chemistry, or costly functional screening of large compound libraries without knowledge of the drug binding site and mechanism (Kharade et al., 2016; Nichols, 2023). The structural insights on existing K_{ATP} pharmacochaperones described above provide a framework for structure-based discovery of new K_{ATP} channel pharmacochaperones. Recently, we conducted a virtual screening study against an RPG-bound K_{ATP} channel structure using AtomNet® (Atomwise-AIMS-Program, 2024), a deep neural network for structure-based drug design and discovery platform, developed by Atomwise Inc., to search for new compounds that bind to the K_{ATP} pharmacochaperone binding pocket (The Atomwise AIMS Program, 2024) (Atomwise-AIMS-Program, 2024; Stafford et al., 2022; Wallach et al., 2015). Specifically, we focused on compounds that can rescue K_{ATP} trafficking mutants without irreversibly inhibiting their function. Here, we report the identification and characterization of a novel K_{ATP} modulator that exhibits pharmacochaperone and reversible inhibitory effects on SUR1/Kir6.2 channels, which we termed Aekatperone (AE-, the initials of the first author of this study, -katperone, K_{ATP} pharmacochaperone). CryoEM structure of SUR1/Kir6.2 K_{ATP} channel in complex with Aekatperone reveals the compound in the predicted binding pocket but with distinct binding features compared to the previously published high affinity inhibitor pharmacochaperones. Our study provides proof of principle for structure-based K_{ATP} channel drug discovery to expand K_{ATP} pharmacology towards mechanism-based and individualized medicine.

Results

Virtual screening for new K_{ATP} channel binders using the AtomNet® technology

CryoEM structures of K_{ATP} channels in complex with pharmacochaperones afford drug discovery opportunities based on structural insights (Ding et al., 2019; Martin et al., 2020; Martin et al., 2019; Sung et al., 2022). Using an Artificial Intelligence (AI) virtual screening system AtomNet® developed by Atomwise (Atomwise-AIMS-Program, 2024; Gniewek et al., 2021; Wallach et al., 2015), we performed virtual screening of ~2.5 million small organic molecules in the Enamine in-stock library against the binding site of a high affinity K_{ATP} inhibitor pharmacochaperone, RPG, resolved in our published RPG-bound K_{ATP} channel (hamster SUR1 plus rat Kir6.2) cryoEM structure (PDB ID 6PZ9; ~3.65 Å) (Atomwise-AIMS-Program, 2024; Martin et al., 2019).

The RPG binding site being screened involves the following residues: R306, Y377, A380, I381, W430, F433, L434, N437, M441, T588, L592, L593, S595, V596, T1242, N1245, R1246, E1249, W1297, R1300 of the SUR1 subunit (chain C in PDB ID 6PZ9), and residue M1, L2, S3, K5, G6, I7 of Kir6.2 (chain D in PDB ID 6PZ9) (Fig. 1A). RPG and all water molecules were removed from the site before screening. Each compound was scored by AtomNet® and the compounds were ranked by their scores (Atomwise-AIMS-Program, 2024; Stafford et al., 2022). Following diversity clustering to minimize selection of structurally similar scaffolds and filtering for oral availability as well as excluding toxicophores (see **Methods** for details), the top 96 predicted binders (Supplementary Table 1) were subjected to subsequent biochemical and functional testing as described below.

Testing top-ranking compounds from virtual screening for pharmacochaperone and gating effects on pancreatic K_{ATP} channels

The study aims to identify new K_{ATP} channel pharmacochaperones that will lead to surface expression and functional recovery of CHI-causing, trafficking-impaired K_{ATP} channels. Accordingly, our initial screening employed a western blot assay that tests the ability of compounds to restore the maturation of SUR1 trafficking mutants. SUR1 contains two N-linked glycosylation sites which are core-glycosylated in the ER. Upon co-assembly with Kir6.2 into a full K_{ATP} complex and its subsequent trafficking through the trans Golgi network, SUR1 becomes complex glycosylated. In western blots, the core- and complex-glycosylated SUR1 proteins appear as a lower and an upper band (Raab-Graham et al., 1999; Zerangue et al., 1999), which are referred to as immature and mature SUR1, respectively. Mutant channel proteins that fail to fold or assemble correctly are retained in the ER such that SUR1 is unable to mature, resulting in an absence of the SUR1 upper band in western blot (Martin et al., 2016; Yan et al., 2004; Yan et al., 2006; Yan et al., 2007). A great majority of such trafficking mutations are located in the N-terminal TMD0 domain of SUR1, which is the primary assembly domain with Kir6.2 (Martin et al., 2020). Most of these mutations are responsive to pharmacochaperone rescue. A well-characterized example is F27S-SUR1 ($SUR1_{F27S}$) (Yan et al., 2007), which prevents SUR1 from acquiring the mature upper band; however, overnight treatment of cells with previously identified pharmacochaperones such as GBC restores the upper band (Yan et al., 2007). We therefore chose $SUR1_{F27S}$ for our initial pharmacochaperone screening (Supplementary Fig. 1A).

To minimize protein expression variations and increase screening efficiency, we transduced rat insulinoma cells INS-1 in a large culture dish with recombinant adenoviruses encoding $SUR1_{F27S}$ (from golden hamster *Mesocricetus auratus*) and wild-type (WT) Kir6.2 (from rat *Rattus rattus*), and then divided the transduced cells into multi-well tissue culture plates for compound testing (see **Methods**). Cells were treated overnight (16 h) with either DMSO (vehicle control), 10 μM of GBC (positive control), or 10 μM of each of the 96 test compounds. $SUR1_{F27S}$ was analyzed by western blot. As expected, in cells treated with DMSO only the immature lower $SUR1_{F27S}$ band was detected; GBC treatment led to the appearance of a strong mature $SUR1_{F27S}$ band (Supplementary Fig. 1B) (Note the low levels of endogenous SUR1 in INS-1 cells was not detectable at the exposure used to detect exogenous $SUR1_{F27S}$). Treatment with some of the test compounds yielded weak or moderate upper $SUR1_{F27S}$ band, suggesting pharmacochaperone effects. We selected three compounds that showed consistent results in two independent screening experiments (Supplementary Fig. 1B) for further testing in a different assay.

The three compounds selected, C24, C27, and C45, correspond to ZINC database (https://zinc.docking.org/) ID: Z1607618869, Z2068224500, and Z1620764636, respectively, and represent diverse chemical scaffolds, as shown in Fig. 1B. Since all known K_{ATP} pharmacochaperones to date also inhibit channel activity, we tested whether the three compounds likewise act as K_{ATP} inhibitors using electrophysiology. For this and subsequent experiments that do not require screening of a large number of compounds, COSm6 cells lacking endogenous K_{ATP} channels were used for transient transfection of WT or mutant K_{ATP} channels. Inside-out patch-clamp recordings of cells expressing K_{ATP} channels (hamster WT SUR1+rat WT Kir6.2) showed that indeed, all three compounds inhibited K_{ATP} channel currents (Supplementary Fig. 2A-C). Upon exposure to the compounds, an immediate reduction in current amplitudes were observed, which was followed by a steady further decline in channel activity. To test reversibility of the inhibitory effects, membrane patches were returned to the K-INT solution without compounds and current recovery was monitored (Supplementary Fig. 2Ai-Ci). Data from these initial studies allowed for an estimate of the potency and reversibility of

these compounds. Of the three compounds Z1620764636 (C45) showed a clear dose-dependent inhibition, with an estimated steady-state IC_{50} between 1-10 μM, and clear current recovery upon compound washout (Supplementary Fig. 2Ci). Compound Z1607618869 (C24) at 5 μM showed > 50% steady-state inhibition and reversibility but increasing the concentrations did not yield consistent further inhibition (Supplementary Fig. 2Aii), which could be due to its poor solubility apparent from visual inspection. Compound Z2068224500 (C27) is the least potent, with an estimated steady-state IC_{50} ~ 20-50 μM, and also the least reversible (Supplementary Fig. 2Bi). Based on these results, we chose to focus further studies on C45, which we named Aekatperone, and will be referred to as such hereinafter.

Aekatperone: a novel K_{ATP} modulator with dual pharmacochaperone and inhibitory actions on pancreatic K_{ATP} channels

Our results from the initial screening experiments suggest Aekatperone as a potential reversible inhibitor pharmacochaperone for surface expression rescue of trafficking-impaired K_{ATP} mutants. The observed current recovery following Aekatperone washout predicts functional recovery of the mutant channels post-treatment. Further biochemical, functional, and structural studies were conducted with Aekatperone obtained from Enamine.

First, we tested the pharmacochaperone effects of Aekatperone on several other trafficking mutations: $SUR1_{A30T}$, $SUR1_{A116P}$, and $SUR1_{V187D}$. These mutations are among the ones that have been shown to not affect the functional properties of K_{ATP} channels (Martin et al., 2016; Yan et al., 2004). COSm6 cells transfected with mutant SUR1 and WT Kir6.2 were treated with DMSO vehicle control or Aekatperone for 16 hours, and mutant SUR1 maturation was monitored by western blotting. Consistent with published studies, western blot of mutants from DMSO treated cells showed clear lower immature band but no or barely detectable upper mature band (Fig. 2A). Overnight treatment with 100 μM Aekatperone led to a clear increase of the mature upper band (Fig. 2A). A detailed dose-response for $SUR1_{A30T}$ showed that the pharmacochaperone effect of Aekatperone was already evident at 10 μM and became more pronounced as the concentration increased, with the effect plateauing between 100 to 200 μM (Fig. 2B). At 200 μM, the intensity of the upper band relative to the total intensity of both lower and upper bands for $SUR1_{A30T}$ was 64.21 ± 3.35% of that observed for WT SUR1 (n = 3, p = 0.0133 by Student's-t test) based on densitometry by ImageJ (Fig. 2B). These results support Aekatperone as a general SUR1-TMD0 K_{ATP} pharmacochaperones.

To demonstrate that the increased mature mutant SUR1 band upon Aekatperone treatment reflects increased surface expression of the mutant channels, we directly monitored K_{ATP} channel surface expression by immunofluorescent staining. In these experiments, COSm6 cells were co-transfected with Kir6.2 and N-terminally FLAG-tagged SUR1. Surface K_{ATP} channels can be detected by incubating cells in medium containing anti-FLAG antibody without cell permeation. As expected, cells transfected with the WT K_{ATP} channel cDNAs showed robust surface staining. In contrast, cells transfected with $SUR1_{F27S}$ or $SUR1_{A30T}$ cDNAs and treated overnight with DMSO showed little surface staining. However, staining of fixed and membrane permeabilized cells transfected with the $SUR1_{F27S}$ or $SUR1_{A30T}$ mutant revealed abundant intracellular fluorescence signal concentrated in the perinuclear region consistent with the mutations causing ER retention of channel proteins (Supplementary Fig. 3, lower panels). Upon Aekatperone treatment, there was a clear increase in the percentage of cells showing surface staining of $SUR1_{F27S}$ or $SUR1_{A30T}$ mutant channels (Supplementary Fig. 3, top panels), providing direct evidence that Aekatperone rescues surface expression of CHI-causing SUR1 trafficking mutations.

In the initial screening, we found that Aekatperone inhibited K_{ATP} currents in inside-out patch-clamp recording experiments (Supplementary Fig. 2C). We further investigated the effects of Aekatperone on K_{ATP} channel response to MgADP stimulation, which is required for physiological activation of K_{ATP} channels in response to glucose deprivation-induced increases in intracellular ADP/ATP ratios (Nichols et al., 1996; Shyng et al., 1998). Increased MgADP concentrations promote NBD dimerization of SUR1 and increase channel opening (Driggers & Shyng, 2023; Wang et al., 2022; Wu et al., 2018; Zhao & MacKinnon, 2021). Because known K_{ATP} inhibitors such as GBC and RPG prevent NBD dimerization by their binding inside a common SUR1 pocket (Ding et al., 2019; Lee et al., 2017; Martin et al., 2019; Martin, Yoshioka, et al., 2017; Wu et al., 2018), against which the virtual screen leading to Aekatperone was conducted, we anticipated that Aekatperone may likewise diminish K_{ATP} stimulation by MgADP. As shown in Fig. 2C and D, robust activation of K_{ATP} channel activity was observed upon addition of 0.5 mM MgADP to the 0.1 mM inhibitory ATP concentration (see **Methods**) as reported previously (Yan et al., 2004). Inclusion of 10 μM Aekatperone occluded the stimulatory effect of MgADP, but MgADP stimulation recovered upon subsequent removal of Aekatperone (Fig. 2C). Thus, like GBC and RPG, Aekatperone blocks channel response to MgADP (Dabrowski et al., 2001; Yan et al., 2006); however, unlike GBC and RPG, Aekatperone's effect is readily reversible. Importantly, the pharmacochaperone effects of Aekatperone on trafficking mutants and reversible inhibitory effect of Aekatperone on channel response to MgADP were also observed in channels formed by human SUR1 and human Kir6.2 (Supplementary Fig. 4), which are highly homologous to hamster SUR1 and rat Kir6.2 at the protein level (95% and 96% respectively). These results demonstrate that Aekatperone is also effective on human K_{ATP} channels.

SUR1 trafficking mutants rescued by Aekatperone show functional recovery upon removal of the compound

The ability of K_{ATP} channels to open in response to hypoglycemia is critical to preventing inappropriate insulin secretion. Based on in vitro electrophysiological experiments showing the reversible inhibitory effect of Aekatperone (Supplementary Figs. 2C, Fig. 2C and D), we hypothesize that trafficking mutants rescued to the cell surface by the drug will open in response to metabolic inhibition, a condition that mimics hypoglycemia, once the drug is removed.

To test the above hypothesis, we employed a Rb^+ efflux assay that allows assessment of channel activity in intact cells (ElSheikh et al., 2024). In this assay, Rb^+, which passes through K_{ATP} channels, is used as a reporter ion to monitor K_{ATP} activity. COSm6 cells transiently expressing WT K_{ATP} channels were preloaded with Rb^+ and treated with metabolic inhibitors (1 mM deoxy-glucose plus 2.5 μg/ml oligomycin, see **Methods**), which activate K_{ATP} channels by lowering intracellular ATP/ADP ratios and mimic hypoglycemia. Rb^+ efflux during a 30 min incubation period was measured in the absence or presence of a range of Aekatperone concentrations (1-200 μM). As shown in Fig. 3A, Aekatperone dose-dependently reduced Rb^+ efflux, with an IC_{50} of 9.23 μM ± 0.36 μM (Fig. 3B). These results are consistent with the electrophysiology data showing inhibition of K_{ATP} currents and MgADP response by Aekatperone in isolated membrane patches (Supplementary Fig. 2C, Fig. 2C). Of note, to ensure Aekatperone is the active compound in our biochemical and functional assays, we tested Aekatperone synthesized from a different commercial source (Acme Bioscience, Palo Alto, California) and confirmed its effects on K_{ATP} channels (Supplementary Fig. 5).

Having established the acute inhibitory effect of Aekatperone on the response of WT K_{ATP} channels to metabolic inhibition, we next asked whether trafficking mutant channels rescued by overnight Aekatperone treatment would show functional recovery following Aekatperone

removal. To test this, COSm6 cells transfected with $SUR1_{F27S}$ and $SUR1_{A30T}$ mutant plasmids were treated for 16 hours with Aekatperone at 10, 30, 50, 100, or 200 μM, or 0.1% DMSO as a vehicle control. Cells were then washed in medium lacking Aekatperone for 30 min before being subjected to Rb^+ efflux assays in the presence of metabolic inhibitors (see **Methods**). Under these conditions, we observed for both mutants a significant increase in Rb^+ efflux in cells treated with Aekatperone in a dose-dependent manner compared with cells treated with 0.1% DMSO (Fig. 3C, D). At 200 μM, Aekatperone overnight treatment followed by washout led to Rb^+ efflux greater than 50% of that observed in cells expressing WT channels and treated with 0.1% DMSO. This is in stark contrast to cells treated overnight with the high affinity inhibitor pharmacochaperone GBC followed by 30 min incubation in medium lacking GBC, where Rb^+ efflux was below that seen in cells treated overnight with the DMSO vehicle control (note in DMSO treated controls, there were still low levels of surface expression of the mutant channels to give rise to the low levels of efflux).

Diazoxide is a K_{ATP} opener and the only pharmacological treatment for CHI. We further evaluated the diazoxide response of mutant K_{ATP} channels rescued by Aekatperone using Rb^+ efflux assay. COSm6 cells expressing either WT channels, $SUR1_{F27S}$, or $SUR1_{A30T}$ trafficking mutants were treated with Aekatperone (100 μM) for 16 hours. Following Aekatperone washout, Rb^+ efflux was measured in the presence of 200 μM diazoxide (see **Methods**; Fig. 3E). As anticipated, untreated cells expressing the trafficking mutants exhibited a low response to diazoxide activation due to the reduced surface expression of K_{ATP} channels, in contrast to cells expressing WT channels (Fig. 3F). Significantly, mutant-expressing cells treated overnight with Aekatperone followed by subsequent drug removal showed much greater diazoxide response, achieving up to 80% of the WT response. These results further support that Aekatperone is a reversible inhibitor pharmacochaperone that rescues surface expression of CHI-causing K_{ATP} trafficking mutants and allows functional recovery and diazoxide response of rescued mutant channels.

Aekatperone shows selectivity towards SUR1-containing channels

In addition to pancreatic K_{ATP} channels formed by SUR1 and Kir6.2, K_{ATP} isoforms formed by assembly of SUR2A or SUR2B with either Kir6.1 or Kir6.2 are present in other tissues and cell types where they have critical physiological functions (Shyng, 2022). Drugs that preferentially target pancreatic K_{ATP} channels would reduce undesired side effects arising from their effects on other K_{ATP} isoforms. As K_{ATP} inhibitor pharmacochaperones exert their effects by binding to a pocket in the SUR subunit, we assessed the acute inhibitory effects of Aekatperone on K_{ATP} isoforms containing Kir6.2 and SUR2A or SUR2B, which are two major splice variants of SUR2, using both electrophysiology and Rb^+ efflux assays.

In electrophysiology experiments, we evaluated whether Aekatperone prevents the ability of SUR2A/Kir6.2 and SUR2B/Kir6.2 channels to respond to MgADP stimulation as seen in SUR1/Kir6.2 channels. Inside-out patch-clamp recordings showed that including 10 μM Aekatperone had no significant effects on MgADP stimulation of SUR2A/Kir6.2 nor SUR2B/Kir6.2 channels (Fig. 4A), indicating SUR2A/Kir6.2 and SUR2B/Kir6.2 channels are relatively insensitive to Aekatperone compared to SUR1/Kir6.2 channels.

Rb^+ efflux experiments were then carried out to assess the effects of Aekatperone on SUR2-containing K_{ATP} channel function in intact cells. COSm6 cells co-transfected with Kir6.2 and WT SUR2A or SUR2B cDNAs were subjected to Rb^+ efflux assays with or without Aekatperone (0-200 μM) in Ringer's solution containing metabolic inhibitors (see **Methods**). The results yielded dose-response curves showing an Aekatperone IC_{50} of 41.22 μM ± 2.22 μM for SUR2A/Kir6.2

channels and 41.85 μM ± 2.08 μM for SUR2B/Kir6.2 channels (Fig. 4B), which are more than four-fold higher than the IC_{50} of 9.2 μM for SUR1/Kir6.2 channels (Fig. 3B). These results further establish the preferential action of Aekatperone on SUR1- versus SUR2A/2B-containing K_{ATP} channels.

Aekatperone binding site revealed by cryoEM structure

Published cryo-EM structures of K_{ATP} channels bound to inhibitor pharmacochaperones, including GBC, RPG and CBZ, have shown that these chemically diverse compounds share a common transmembrane domain binding pocket in SUR1 but have distinct chemical interactions with the channel (Ding et al., 2019; Martin, Kandasamy, et al., 2017; Martin et al., 2019; Martin, Yoshioka, et al., 2017; Wu et al., 2018). We anticipate Aekatperone to bind to the same pocket as the structure of this pocket was used for the initial virtual screening. Because AtomNet® evaluates each compound based on an ensemble of possible poses, it remains uncertain how Aekatperone interacts with the channel. To directly visualize how Aekatperone interacts with the channel we determined the cryoEM structure of K_{ATP} channels in the presence of 50 μM Aekatperone, using our published cryoEM sample preparation, imaging, and data processing workflow with specific modifications (Driggers et al., 2024; Driggers & Shyng, 2021; Martin, Kandasamy, et al., 2017; Martin et al., 2019; Martin, Yoshioka, et al., 2017) (see **Methods** and Supplementary Fig. 6).

3D reconstruction of cryoEM particles of channels incubated with Aekatperone yielded a map with an overall resolution of 4.1 Å. A model built from the map shows a closed Kir6.2 channel pore with a pore radius of ~0.75 Å at the helical bundle crossing residue F168 and an inward-facing SUR1 with NBDs separated, resembling other inhibitor-bound K_{ATP} channel structures reported to date (Fig. 5A). A clear non-protein density consistent with the size of Aekatperone (MW: 399.52 g/mol) was observed in a transmembrane pocket above NBD1 in the ABC core of SUR1 (Fig. 5 B-D). We have previously shown that this same pocket accommodates other inhibitor pharmacochaperones including GBC, RPG, and CBZ (Martin et al., 2019). Moreover, as in the structures of K_{ATP} bound to GBC, RPG, or CBZ, we observed clear cryoEM density corresponding to the Kir6.2 distal N-terminal peptide domain (KNtp) in between the two TM bundles of the SUR1-ABC core, with the very N-terminus of Kir6.2 contacting the bound Aekatperone (Fig. 5A).

Aekatperone comprises a cyclohexane ring, a pyrazole, a sulfonamide moiety, a benzene ring, and an imidazole group (Fig. 1B). The preferred binding conformation, which accounted for the physical chemical properties of the compound and its surrounding interacting protein residues as well as fit to the cryoEM density, is shown in Fig. 5B,C. In this structural model, the cyclohexyl moiety of Aekatperone is aligned with S1238 on the cytoplasmic end of the binding pocket, and the imidazole group is oriented towards the extracellular end of the binding pocket, interacting with the distal part of KNtp. The pyrazole moiety has its two nitrogen atoms coordinated by T1242 and N1245, while the sulfonyl moiety is oriented towards R1246 and R1300, each interacts with one of the two oxygens of the sulfonyl group. Moreover, the benzene ring of Aekatperone forms a π–π stacking interaction with Y377 of SUR1, and a series of hydrophobic interactions contributed by TM helices from both TMD1 (TM6, 7) and TMD2 (TM16, 17) help stabilize the benzene and cyclohexyl groups. Interestingly, unlike GBC and RPG, the binding of both involves R306 of SUR1, Aekatperone does not reach far into the extracellular end of the pocket to interact with R306 (Fig. 5B,C; Supplementary Fig. 7).

In examining the cryoEM density-Aekatperone model fitting, it is noticeable that the imidazole group next to KNtp lacks clear matching cryoEM density (Fig. 5B-D). To investigate the dynamic

behavior of Aekatperone in the SUR1 cavity, which may explain why the cryoEM density only partially covers the modeled structure of Aekatperone, we employed molecular dynamics (MD) simulations (Supplementary Fig. 8). During MD simulations of Aekatperone in its SUR1 binding pocket Aekatperone remained within the pocket throughout the 500 ns simulation time in all five runs (a total of 2.5 μs) but exhibited some flexibility. To characterize the dynamics of Aekatperone, we divided its structure into five parts and analyzed the movement of each part individually. The positions of the centers of mass for each part, shown in corresponding colors in Fig. 6A, indicate that while the positional distributions of most groups are relatively localized, group e, which corresponds to the imidazole ring, displays considerable conformational freedom. This is further illustrated in Fig. 6B, where we calculated the standard deviation of the distances from their initial positions.

To some extent, the ligand's mobility is related to the flexibility of the amino acids within the surrounding pocket. The potential influence of conformational changes of SUR1 was reduced by aligning the trajectory on the Cα atoms of the pocket surrounding the ligand. However, side-chain mobility might still play a role. Therefore, we analyzed the ligand's surroundings and specifically investigated the frequency of the ligand remaining in close contact with the pocket amino acids. Fig. 6C shows the residues that stayed near the ligand for over 40% of the trajectory duration. Despite the ligand's mobility, some interactions remain at 80% or even 100%. These include the interaction of fragment a (brown) with F433, I381, and S1238, nearly 100% interaction of the sulfonyl group (yellow) with R1246, and slightly lesser interaction of group d (dark blue) with I381 and Y377. Y377 also participates to a slightly lower extent in binding fragment e. By sampling the available volume, the fragment e forms temporary interactions with KNtp amino acids (mainly M1 and S3), which also exhibit considerable conformational freedom within the pocket (Supplementary Fig. 9). An example snapshot from the simulation, showing Aekatperone in the SUR1 pocket and its interactions with SUR1 and KNtp amino acids, is depicted in Fig. 6D and E, in a side and top views, respectively.

Functional validation of the Aekatperone binding site model

To validate the above binding site model, we mutated a subset of Aekatperone-binding residues, including Y377, R1246, and R1300 to alanine (Fig. 7A) and tested the effects of the mutation on channel response to the acute inhibitory effect of Aekatperone by Rb^+ efflux assays. R306, which is predicted not to interact with Aekatperone was also evaluated as a control. Consistent with our structural model, Y377A, R1246A, and R1300A all significantly decreased the dose-dependent inhibitory effects of Aekatperone (Fig. 7B). In particular, the Y377A and R1300A mutations are detrimental to the ability of Aekatperone to inhibit the channel even at the highest concentration of Aekatperone (50 μM) tested, indicating a crucial role of these two residues. By contrast, R306A had little effects on channel inhibition by Aekatperone, consistent with a lack of R306 involvement in Aekatperone binding.

In the Aekatperone binding site model, S1238 and T1242 of SUR1 lie next to the cyclohexyl and the pyrazole moieties (Figs. 5B,C, 7A; Supplementary Fig. 7). These two residues correspond to Y1205 and S1209 respectively in SUR2A and SUR2B. The substitution of the bulky tyrosine residue for serine at the SUR1-1238 position is expected to cause a steric interference with the bound drug, whereas serine substitution for threonine at the SUR1-1242 position requires serine to be in one of three possible rotomeric positions to allow interaction with the pyrazole group. We reasoned that these two amino acid substitutions in SUR2A/2B may account for the reduced Aekatperone inhibition seen in SUR2 isoforms compared to SUR1. To test this, we conducted Rb^+ efflux assays in COSm6 cells expressing Kir6.2 and WT SUR1 or SUR1 with S1238Y and T1242S double mutation. The inhibitory effect of Aekatperone was significantly reduced by

combined S1238Y and T1242S mutation compared to WT control at the 10-50 μM concentrations tested (Fig. 7B). These findings further support the Aekatperone binding site model and offer a structural explanation for the lower sensitivity of the SUR2 channel isoform to the compound compared with the SUR1 isoform.

An additional structural element predicted to participate in Aekatperone binding based on our model is the distal N-terminus of Kir6.2, or KNtp (Figs. 5A, 6C, 8A, B). In particular, the imidazole group of Aekatperone is in close proximity to the cryoEM density corresponding to the distal end of KNtp and may directly interact with KNtp residues (Figs. 5B and C, 6C, 8A and B; Supplementary Fig.9). To test the involvement of KNtp in channel inhibition by Aekatperone, we assessed the effects of deleting the N-terminal residues of Kir6.2 on channel response to 10, 20, 30, or 50 μM of the drug using Rb^+ efflux assays in COSm6 cells transiently co-transfected with $SUR1_{WT}$ along with $Kir6.2_{WT}$ or Kir6.2 lacking the distal 2-5 or 2-10 amino acids of Kir6.2 (referred to as $Kir6.2\Delta_{N5}$ or $Kir6.2\Delta_{N10}$). Both $Kir6.2\Delta_{N5}$ and $Kir6.2\Delta_{N10}$ significantly attenuated the inhibitory effect of Aekatperone at all four concentrations (Fig. 8C). These results are in agreement with a role of KNtp in the binding of Aekatperone and/or transducing the effect of Aekatperone binding to channel closure. Taken together, the above functional data provides strong support for the Aekatperone binding site model derived from the cryoEM density map.

Discussion

Here, we report the discovery and characterization of a new pancreatic-selective K_{ATP} channel binder with dual pharmacochaperone and inhibitory effects. The compound, which we name Aekatperone, rescues K_{ATP} channel trafficking mutants to the cell surface. While Aekatperone also inhibits channel activity, its inhibitory effect is readily reversible upon washout to allow functional recovery of rescued channels. These properties distinguish Aekatperone from existing high affinity K_{ATP} inhibitory ligands with pharmacochaperone actions and make it a suitable candidate for combating CHI caused by K_{ATP} trafficking defects. The cryoEM structure reveals that although Aekatperone sits in the same pocket that has been previously identified for high affinity inhibitors, it adopts a distinct binding position which may underlie its reduced apparent affinity and reversibility. Our study provides proof-of-principle for AI-assisted and structure-based K_{ATP} channel drug discovery tailored to specific channel defects.

AI-aided virtual screening in drug discovery

Compared to physical high throughput screening of large compound libraries, computational virtual screening offers a faster and more cost-effective alternative approach to drug discovery. However, until recently computation-based drug development has been limited due to the scarcity of high resolution protein structures especially for membrane proteins. The rapid rise in the number of high resolution cryoEM structures of membrane proteins in the past decade and the mechanistic insights from these structures present an exciting opportunity for structure-based drug discovery. Taking advantage of cryoEM structures of the pancreatic K_{ATP} channel bound to several known molecules with pharmacochaperone and inhibitory effects, we set out to search for additional small molecule binders for the pocket using the AI-aided virtual screening platform AtomNet®, developed by Atomwise Inc. Out of the 96 top ranking compounds, at least 3 with distinct scaffolds showed in the initial single-dose experimental screen promising pharmacochaperone and inhibitory effects on the channel to warrant follow-up studies. To our knowledge, this is the first structure-based virtual screening study conducted for K_{ATP} channels. In contrast to other recent large scale structure-based virtual screening studies involving docking of more than a billion compounds in target proteins such as GPCRs and CFTR (Fink et al., 2022; Grotsch et al., 2024; Liu et al., 2024), our AI-based virtual screening against the K_{ATP}

channel focused on ~2.5 millions compounds in the smaller Enamine library, which can be readily purchased for experimental testing. The success in identifying several compounds validated by functional assays in our study illustrates the cost-effectiveness of this approach in drug discovery for K_{ATP} channels. This approach has also been shown effective for other targets as recently documented in the Atomwise AIMS program (Atomwise-AIMS-Program, 2024). Thus, AI-aided structure-based virtual screening is emerging as a promising strategy for discovering novel therapeutics, a particularly important drug discovery development for rare diseases.

Binding site comparison between Aekatperone and other K_{ATP} inhibitors

Early structure-activity relationship studies of K_{ATP} targeting drugs such as first and second generations of sulfonylureas, exemplified by tolbutamide and glibenclamide respectively and glinides including repaglinide, along with comparative mutagenesis studies between SUR1 and SUR2 have led to a binding site model for K_{ATP} inhibitors (Quast et al., 2004). In this model, the high affinity sulfonylurea glibenclamide comprises two binding sites: site A which accommodates the sulfonylurea part of the molecule, and site B which accommodates the benzamido end of the molecule, with the central phenyl ring shared between site A and site B (Quast et al., 2004). Tolbutamide, which binds the channel with 1000-fold lower affinity than glibenclamide and comprises only the phenyl ring and sulfonylurea group is thought to bind site A, whereas repaglinide which contains a phenyl ring and a benzamido moiety is thought to bind site B. Site A involves S1238 in SUR1, which is substituted by a tyrosine in SUR2. Mutation of SUR1 S1238 to Y abolishes tolbutamide binding, lowers glibenclamide binding affinity and renders glibenclamide inhibition reversible, but has no effect on repaglinide binding. This model has been largely confirmed by recent cryoEM structures (Driggers & Shyng, 2023; Wu et al., 2020) (see Supplementary Fig.7). According to this model, Aekatperone would be classified as a site A ligand. This is supported by structural data showing Aekatperone occupying the space corresponding to the site A part of glibenclamide, and by mutagenesis data showing that the S1238Y-SUR1 mutation compromises channel inhibition by Aekatperone. Interestingly, whereas tolbutamide and Aekatperone, both site A ligands block the channel with lower potencies (IC_{50} ~23 μM and 9 μM respectively) (ElSheikh et al., 2024) and are reversible, another site A ligand, mitiglinide (Wang et al., 2022) (see Supplementary Fig.7D) is a much more potent and nearly irreversible inhibitor with an IC_{50} in the low nM range (Reimann et al., 2001). Thus, site A ligands can exhibit a wide range of potencies. MD simulations of the Aekatperone binding site revealed dynamic interactions between the drug and amino acids in the channel from both subunits. Whether these dynamics underlie the lower affinity and reversibility of Aekatperone remains to be determined. Additional MD simulations and structure-function correlation studies may shed light on the mechanisms that dictate the apparent affinity and reversibility observed for the known inhibitor pharmacochaperones.

The Aekatperone bound pancreatic K_{ATP} structure also reveals that aside from S1238, another residue T1242, which is altered to a serine in SUR2, contributes to ligand binding and the ~4-5 fold higher selectivity of the ligand for SUR1 vs SUR2 channels. Moreover, our structural and functional data point to a role of Kir6.2-N terminus in Aekatperone interaction and action. The expanding ligands and structure-function information will facilitate rational design of drugs with specific properties to meet a wide-range of medical needs arising from K_{ATP} dysfunction.

Implications for congenital hyperinsulinism

As a rare disease, CHI has not been a major target for drug development. The majority of CHI with known genetic causes are due to loss of function mutations in the K_{ATP} channel genes (Hewat et al., 2022; Stanley, 2016). Nearly half of CHI-K_{ATP} mutations that have been studied

prevent surface expression of the channel, rendering them unable to respond to the K_{ATP} channel opener diazoxide, the mainstay medical treatment available for CHI (ElSheikh & Shyng, 2023). Unlike cystic fibrosis, in which 90% patients carry one or two copies of a highly prevalent trafficking mutation ΔF508 in CFTR (Cutting, 2015), there is no single highly prevalent mutation in the K_{ATP} channel that underlies channel trafficking defects. However, we have shown that K_{ATP} channel trafficking mutations are concentrated in SUR1-TMD0 (ElSheikh & Shyng, 2023; Martin et al., 2020). K_{ATP} inhibitors, including tolbutamide, glibenclamide, repaglinide, and carbamazepine, as well as Aekatperone described here rescue trafficking SUR1-TMD0 trafficking mutants to the cell surface. Thus, inhibitor pharmacochaperones would have general applications to a significant number of CHI patients.

An additional challenge for the pharmacochaperone therapeutic approach is the inhibitory nature of the K_{ATP} pharmacochaperones. Glibenclamide and repaglinide bind K_{ATP} with such high affinity that they prevent functional recovery of rescued channels. Carbamazepine, while more reversible, has multiple known ion channel targets including Na_v, Ca_v, and NMDA receptors (Ambrósio et al., 1999; Gambeta et al., 2020; Matsumoto et al., 2015; Tikhonov & Zhorov, 2017). Tolbutamide would be suitable due to its low binding affinity and reversibility; however, it has long been taken off market due to concerns over its adverse cardiovascular effects (Ashcroft, 2005; Schwartz & Meinert, 2004). Thus, new K_{ATP} pharmacochaperones are needed. CryoEM structures suggest that K_{ATP} inhibitors bind to the SUR1 ABC core domain and stabilizes SUR1-Kir6.2 interactions to promote mutant channel assembly (Martin et al., 2019). However, stabilization of this interface also restricts the movement of the Kir6.2 cytoplasmic domain towards the open conformation (Driggers et al., 2024; Martin et al., 2019; Sung et al., 2022; Wu et al., 2018). As such, the principal challenge in the clinical use of pharmacological chaperones for patients with CHI lies in balancing channel activity enhancement by boosting surface expression with activity inhibition via gating. Our efforts has therefore focused on identifying novel pharmacochaperones with more reversible inhibitory effects. Aekatperone is a promising lead as it fits the profile of a reversible inhibitor pharmacochaperone, and shows little effects on SUR2 K_{ATP} isoforms in the concentration range for its pharmacochaperone effects on pancreatic K_{ATP} channels. Significantly, we showed that upon Aekatperone overnight rescue and quick washout, diazoxide greatly enhanced efflux in cells transfected with trafficking mutant channels to nearly 80% of that observed for WT channels. A dosing regiment incorporating diazoxide and a reversible inhibitor pharmacochaperone such as Aekatperone to harness the channel potentiating effect of diazoxide would further enhance the therapeutic effect of the pharmacochaperone.

Limitations and future directions

We show that Aekatperone is ~4-5 fold more selective for SUR1-containing pancreatic K_{ATP} over SUR2A/B containing K_{ATP} based on functional studies. The selectivity suggests clinical use may involve fewer side effects due to isoform cross reactivity. However, we have not tested the compound against other protein targets, therefore potential off-target effects remain. In this regard, it is interesting that nateglinide, a antidiabetic glinide drug which would be predicted to bind the same pocket as Aekatperone, has been shown to be a low micromolar agonist for the human itch GPCR MRGPRX4 (Cao et al., 2021).

Compared to ultra-large library docking of over a billion make-on-demand compounds, our focused approach on a commercially available smaller compound library may miss potential scaffolds that will bind to our target and yield the desired biological effects. We envision the AI-based screening can be scaled up to cover even more diverse molecules.

Finally, we demonstrate surface expression and functional rescue of K_{ATP} channel trafficking mutants by Aekatperone in a cell culture experimental system. Translation of this finding to clinical applications will require many more studies using relevant cell and animal models. Nonetheless, our study offers a framework for structure and mechanism based drug development for K_{ATP} channels.

Methods

Virtual screening using the AtomNet® platform

The virtual screening was carried out using AtomNet®, within the framework of Atomwise's academic collaboration program known as Artificial Intelligence Molecular Screen (AIMS). AtomNet® is a deep neural network for structure-based drug design and discovery (Gniewek et al., 2021; Wallach et al., 2015). An Enamine in-stock library of ~2.5 millions commercially available compounds was first filtered using the Eli Lilly medicinal chemistry filters to remove potential false positives from the group, including aggregators, autofluorescers, and pan-assay interference compounds (PAINS) (Baell & Holloway, 2010; Bruns & Watson, 2012). The filtered library was then virtually screened using the CryoEM structure of the K_{ATP} channel bound to repaglinide (PDB ID: 6PZ9, ~3.65 Å) (Martin et al., 2019), targeting the binding site within the central cavity of the SUR1 subunit of the K_{ATP} channel (Fig. 1A). Molecules with greater than 0.5 Tanimoto similarity in ECFP4 space to any known binders of the target and its homologs within 70% sequence identity were excluded from the virtual screen. For each small molecule, we generated an ensemble of binding poses within the target site. These poses were then scored utilizing the AtomNet® technology, enabling ranking of molecules based on their predicted affinity. To ensure diversity in the selected compounds and to minimize the selection of structurally similar scaffolds, the top 30,000 molecules were clustered using the Butina algorithm (Butina, 1999). Furthermore, we applied filters to assess oral availability and to eliminate compounds containing undesirable substructures and molecular properties known as toxicophores. Detailed description of the AIMS screening protocol can be found in recent literature (Atomwise-AIMS-Program, 2024). The top-ranking compounds predicted to exhibit high affinity binding were subsequently purchased for experimental testing.

Compounds for functional screening

Top-ranking 96 compounds were purchased from Enamine (Kyiv, Ukraine). To ensure that the Aekatperone biological effects we observed on K_{ATP} channels were not due to minor contaminants, we also purchased Aekatperone synthesized from a different commercial source, Acme Bioscience, Inc. (Palo Alto, CA, USA).

Expression constructs

Hamster SUR1 was tagged with a FLAG epitope (DYKDDDDK) at the extracellular N-terminus (referred to as FLAG-SUR1) and the cDNA cloned into the pECE vector. We have shown in previous studies that these epitope tags do not affect the trafficking or function of the channel (Cartier et al., 2001; Lin et al., 2005). WT rat Kir6.2 cDNA was cloned into pcDNA1/Amp, as described previously (Cartier et al., 2001). Point mutations to FLAG-SUR1 were introduced using the QuikChange site-directed mutagenesis kit (Agilent Technologies). All mutations were confirmed by DNA sequencing, and mutant clones from two independent PCR reactions were analyzed in all experiments to avoid false results caused by undesired mutations introduced by PCR. For experiments involving human K_{ATP}, WT or mutant human SUR1 cDNA and WT human Kir6.2 cDNA were cloned into pCMV6b and pcDNA3.1(+) vectors respectively. Also, WT rat SUR2A and WT rat SUR2B that were cloned into pcMV6 were used in experiments that aimed to test isoform specificity. Construction of adenoviruses carrying K_{ATP} subunits cDNAs was as

described previously (Lin et al., 2008). The hamster FLAG-SUR1$_{F27S}$ recombinant adenovirus was made using a modified pShuttle plasmid (AdEasy kit, Agilent Technologies) containing a tetracycline-inducible promoter and requires co-infection of a virus carrying the cDNA encoding a tetracycline-inhibited transactivator (tTA) for expression. Recombinant viruses were amplified in HEK293 cells and purified according to the manufacturer's instructions.

Transduction of INS-1 cells *with recombinant adenoviruses for experimental screening of the top 96 scoring compounds from the virtual screening*

INS-1 cell clone 832/13 (Hohmeier et al., 2000), a rat insulinoma cell line (kindly provided by Dr. Christopher Newgard) were plated in 15 cm plates and cultured for 24 h in RPMI 1640 with 11.1 mM D-glucose (Invitrogen) supplemented with 10% fetal bovine serum, 100 units/ml penicillin, 100 µg/ml streptomycin, 10 mM HEPES, 2 mM glutamine, 1 mM sodium pyruvate, and 50 µM β-mercaptoethanol (Hohmeier et al., 2000). Cells at ~70% confluency were washed once with Dulbecco's Phosphate Buffered Saline; Sigma-Aldrich) and then incubated for 2 h at 37 °C in Opti-MEM reduced serum medium (Gibco) and a mixture of viruses including the tTA virus, the tTA-regulated hamster FLAG-SUR1$_{F27S}$ virus and the rat Kir6.2$_{WT}$ virus as described previously (Driggers & Shyng, 2021; Lin et al., 2005; Lin et al., 2008). The multiplicity of infection (MOI) for each virus was determined empirically and the amount of virus needed to achieve the necessary MOI was calculated as follows: (Number of cells in dish or well x desired MOI)/Titer of the virus stock (pfu/ml) (Driggers & Shyng, 2021). After 120 minutes, INS-1 growth medium was added and the cells were incubated at 37°C until they reached the appropriate density for the various experiments. Cells were then incubated for an additional 16-17h in RPMI 1640 with 10% FCS containing either DMSO, glibenclamide or each of the top scoring (96) compounds before harvesting for immunoblotting.

Transfection of COSm6 cells with recombinant DNA

COSm6 cells plated in 6-well tissue culture plates at ~70% confluency were transfected with 1.2 µg of WT or mutant SUR1, SUR2A, or SUR2B and 1.2 µg of Kir6.2 per well using FuGENE 6 (Promega) according to the manufacturer's directions. It is essential to initially mix the plasmids in Opti-MEM in a separate tube before adding the FuGENE® to ensure the uptake of multiple plasmids required for K_{ATP} channel expression by the cell.

Immunoblotting

INS-1 cells transduced with recombinant adenoviruses or COSm6 cells transfected with SUR1 and Kir6.2 cDNAs were lysed in lysis buffer (50 mM Tris·HCl, pH 7.0, 150 mM NaCl, and 1% TritonX 100, with Complete^{TR} protease inhibitors) on ice for 30 min. Cell lysate was centrifuged at 16,000x *g* for 5 min at 4°C, and an aliquot of the supernatant was run on SDS-PAGE and transferred to nitrocellulose membrane. The membrane was probed with a rabbit anti-SUR1 serum raised against a C-terminal peptide of SUR1 (KDSVFASFVRADK) (Yan et al., 2007), followed by incubation with horseradish peroxidase-conjugated secondary antibodies (Amersham Biosciences), and visualized by enhanced chemiluminescence (Super Signal West Femto; Pierce). Tubulin was also probed and served as a loading control.

Patch-clamp recording

COSm6 cells were transfected with SUR1, SUR2A or SUR2B and Kir6.2 cDNAs along with cDNA encoding the green fluorescent protein to identify transfected cells. Cells were plated onto glass coverslips 24 h after transfection and recordings made in the following two days. To test the acute effect of the drug, cells were subjected to inside-out patch voltage-clamp recording in solutions containing 1 mM ATP, 0.1 mM ATP or 0.1 mM ATP plus 0.5 mM ADP with or without the drug Aekatperone (10 µM), $MgCl_2$ was added such that the free Mg^{2+}

concentration of the solutions was ~1 mM (Shyng & Nichols, 1998). Micropipettes were pulled from non-heparinized Kimble glass (Fisher Scientific) on a horizontal puller (Sutter Instrument, Novato, CA) with resistance typically ~1-2 MΩ. The bath (intracellular) and pipette (extracellular) solutions into which membranes were excised, were K-INT: 140 mM KCl, 10 mM K-HEPES, 1 mM K-EDTA, pH 7.3. ATP and ADP were added as potassium salts. Inside-out patches of cells bathed in K-INT were voltage-clamped with an Axopatch 1D amplifier (Axon Instruments). Recording was performed at room temperature (Devaraneni et al., 2015) and currents were measured at a membrane potential of -50 mV. Inward currents in all figures are shown as upward deflections. Data were analyzed using pCLAMP10 software (Axon Instrument). Off-line analysis was performed using Clampfit and GraphPad. Data were presented as mean ± standard error of the mean (SEM).

Immunofluorescence staining

COSm6 cells transfected with WT Kir6.2 and WT, A30T or F27S FLAG-SUR1 were plated on coverslips one day before the experiment and treated overnight with DMSO, or Aekatperone. To label channels expressed at the cell surface, cells were washed once with ice-cold phosphate buffered saline (PBS): 137 mM NaCl, 2.7 mM KCl, 10 mM Na_2HPO_4, 1.8 mM KH_2PO_4, pH 7.4 and then incubated with M2 anti-FLAG antibody (10 µg/ml in Opti-MEM plus 0.1% BSA) for 1 hour at 4°C. Cells were washed with ice-cold PBS and fixed with ice-cold 4% paraformaldehyde for 10 min on ice, and washed three times with cold PBS. Fixed cells were then incubated in blocking buffer (PBS + 2% BSA + 1% normal goat serum) for 1 hour, followed by incubation with Alexa Fluor 546-conjugated goat anti-mouse secondary antibody (Invitrogen; 1:300 dilution in blocking buffer) for 1 hour at room temperature. For staining of total cellular FLAG-SUR1, the cells were fixed with ice-cold 4% paraformaldehyde for 10 min on ice before incubation with anti-FLAG antibody followed by Alexa Fluor 546-conjugated goat anti-mouse secondary antibody. The cells were then washed twice with PBS and the coverslips were mounted on microscope slides using Vectashield Mounting Medium for Fluorescence with DAPI. Cells were viewed using a Olympus confocal microscope.

Rb^+ Efflux Assay

COSm6 cells were transiently transfected with various combinations of WT or mutant SUR1 and Kir6.2 cDNAs. Untransfected cells were included as background control. Cells were cultured in medium containing 5.4 mM RbCl overnight. The next day, cells were washed quickly twice in PBS with no RbCl. For experiments testing the acute inhibitory effects of Aekatpeone (Figs. 3A, 4B, Supplementary Figs. 4C, 5), Rb^+ efflux was measured by incubating cells in Ringer's solution (5.4 mM KCl, 150 mM NaCl, 1 mM $MgCl_2$, 0.8 mM NaH_2PO_4, 2 mM $CaCl_2$, 25 mM HEPES, pH 7.2) with metabolic inhibitors (2.5 µg/ml oligomycin and 1 mM 2-deoxy-D-glucose) and combined with the drug, for 30 minutes at 37°C (ElSheikh et al., 2024).

For experiments testing the pharmacochaperone effects of Aekatperone (Fig. 3C, D), the drug was added to the RbCl-containing media overnight and an additional wash step in RbCl wash buffer (5.4 mM RbCl, 150 mM NaCl, 1 mM $MgCl_2$, 0.8 mM NaH_2PO_4, 2 mM $CaCl_2$, 25 mM HEPES, pH 7.2) for 30 minutes at 37°C was included to remove Aekatperone prior to the efflux assay. Rb^+ efflux was measured by incubating cells in Ringer's solution with only metabolic inhibitors without Aekatperone (ElSheikh et al., 2024). Similarly, for experiments evaluating the role of Aekatpeone in enhancing diazoxide response (Fig. 3E,F), Aekatpeone was included in the RbCl-containing medium overnight with an additional drug washout step, and the efflux was conducted in Ringer's solution containing 200 µM diazoxide.

For all efflux experimentss, efflux solution was collected at the end of a 30 min incubation period and cells were lysed in Ringer's solution plus 1% Triton X-100. Rb^+ concentrations in both the efflux solution and cell lysate were measured using an Atomic Adsorption Instrument Ion Channel Reader (ICR) 8100 from Aurora Biomed. Fractional Rb^+ efflux was calculated by dividing Rb^+ in the efflux solution over total Rb^+ in the efflux solution and cell lysate. Fractional Rb^+ efflux from untransfected COSm6 cells was subtracted from other experimental readings. The data were normalized to the fractional Rb^+ efflux of cells expressing WT channels treated with metabolic inhibitors without any drugs, unless specified otherwise. For each experiment, technical duplicates were included, and the average value was used as the experimental result. At least three separate transfections were performed for each experimental condition as biological repeats, as detailed in the figure legends (number of biological repeats represented as small circles on the graphs). Data are presented as mean ± SEM.

Protein expression and purification for cryoEM

K_{ATP} channels were expressed and purified as described previously (Martin, Yoshioka, et al., 2017). Briefly, eight 15 cm tissue culture plates of INS-1 cells clone 832/13 were transduced with the tTA adenovirus and recombinant adenoviruses carrying hamster FLAG-SUR1 and rat Kir6.2 cDNAs (Driggers & Shyng, 2021). After growing for approximately 48 hours post-infection, cells were washed with PBS and harvested by scraping. Cell pellets expressing FLAG-SUR1 and Kir6.2 were frozen in liquid nitrogen and stored at -80°C until purification.

For purification, cells were resuspended in hypotonic buffer (15 mM KCl, 10 mM HEPES pH7.5) with protease inhibitor, PI (cOmplete™ Mini Protease inhibitor, Roche, Basel, Switzerland), and 1.0 mM ATP and lysed by Dounce homogenization. The total membrane fraction was prepared, and membranes were resuspended in Membrane Solubilization Buffer (MSB; 200 mM NaCl, 100 mM KCl, 50 mM HEPES pH 7.5) containing PI, 1 mM ATP, 4% w/v trehalose, and 50 µM Aekatperone and solubilized with 0.5% Digitonin. The soluble fraction was incubated with anti-FLAG M2 affinity agarose for 12 hours, washed three times with MSB + 0.5% Digitonin + PI + ATP+ Aekatperone solution, and eluted for 60 minutes at 4°C with 1.0 mL of a solution like the final wash but containing 0.25 mg/mL FLAG peptide. The eluted sample was loaded onto a Superose 6 10/300 column run by an ÄKTA FPLC (Cytiva Life Sciences), and 0.5 mL fractions were collected. Fractions corresponding to the hetero-octameric K_{ATP} channels were collected and concentrated to a volume of ~60 µL and used immediately for cryo grid preparation.

Sample preparation and data acquisition for cryoEM analysis

Using a Vitrobot Mark III (FEI), a 3 µL aliquot of purified and concentrated K_{ATP} channel was loaded onto Lacey Carbon grids that had been glow-discharged for 60 s at 15 mA with a Pelco EasyGlow. The grid was blotted for 2 s (blot force -4; 100% humidity at 4°C) and cryo-plunged into liquid ethane cooled by liquid nitrogen to flash vitrify the sample.

Single-particle cryo-EM data was collected on a Titan Krios 300 kV cryo-electron microscope (ThermoFisher Scientific) in the Pacific Northwest CryoEM Center (PNCC), with a multi-shot strategy using beam shift to collect 19 movies per stage shift, assisted by the automated acquisition program SerialEM. Movies were recorded on the Gatan K3 Summit direct-electron detector in super-resolution mode with Fringe-free imaging, post-GIF (20eV window), at 81,000x magnification (calibrated image pixel-size of 1.0515 Å; super-resolution pixel size 0.52575 Å); nominal defocus was varied between -1.0 and -2.5 µm across the dataset. The dose rate was kept around 17 $e^-/Å^2$/sec, with a frame rate of 23 frames/sec, and 74 frames in each movie (i.e. 3.2 sec exposure time/movie), which gave a total dose of approximately 55 $e^-/Å^2$. Two grids that were prepared in the same session using the same protein preparation were used for data

collection, and from these two grids 21,012 movies were recorded. As Lacey carbon grids do not have a regular array of holes, many of the movies contain a large fraction of carbon support in the images.

Image processing and model building

Super-resolution dose-fractionated movies were gain-normalized by inverting the gain reference in Y and rotating upside down, corrected for beam induced motion, aligned, and dose-compensated using Patch-Motion Correction in cryoSPARC2 (Punjani et al., 2017) and binned with a Fourier-crop factor of ½. Parameters for the contrast transfer function (CTF) were estimated from the aligned frame sums using Patch-CTF Estimation in cryoSPARC2. The resulting 21,012 dose-weighted motion-corrected summed micrographs were used for subsequent cryo-EM image processing. Particles were picked automatically using template-based picking in cryoSPARC2 based on 2D classes obtained from cryoSPARC live during data collection. Incorrect particle picks containing carbon edges, or features on the support carbon, were cleaned by multiple rounds of 2D classification in cryoSPARC2. The resulting stack contained 78,490 particles, which were extracted using a 512^2 pixel box and were used for ab initio reconstruction in C1 followed by homogeneous refinement in C1, which gave a Gold-standard FSC resolution cutoff (GSFSC) (Rosenthal & Henderson, 2003) of about 6.3 Å. Homogeneous refinement with C4 symmetry imposed gave a GSFSC cutoff of 4.8 Å resolution. Reconstruction from all particles shows an NBD-separated SUR1 with a closed Kir6.2 pore and cryoEM density at the putative Aekatperone binding site.

To assess conformational heterogeneity within the analyzed particles and to improve the density for Aekatperone, particles were subjected to 4-fold symmetry expansion at the C4 axis. A mask covering the Kir6.2 tetramer, TMD0 of the four SUR1 subunits, plus a large volume surrounding one of the full SUR1 subunits, to have a large region covering all possible SUR1 locations (Supplementary Fig. 6A), was generated using Chimera and used as a focused map to conduct 3D classification of these 313,960 symmetry-expanded particles without particle alignment in cryoSPARC2. This yielded three dominant classes all with closed Kir6.2 pores and separated SUR1-NBDs that differed in the position of the Cytoplasmic Domain (CTD) of Kir6.2 (Supplementary Fig. 6A). A class of 125,416 symmetry-expanded particles in the CTD-up conformation gave a 4.1 Å resolution reconstruction (masked), and the CryoEM density map from this reconstruction was used to build a model of the K_{ATP} channel bound to Aekatperone. In this reconstruction of the full K_{ATP} channel particle, there is sufficient density to define helical positions and domain positions that are similar to RPG or GBC-bound structures previously published. The transmembrane helices have higher local resolution than the dynamic NBDs and loop regions (Supplementary Fig. 6B).

To create an initial structural model, PDB ID 7TYS had ligands removed and then was fit into the reconstructed density for the full K_{ATP} channel particle using Chimera, and then refined in Phenix as separate rigid bodies corresponding to TMD (32-171) and CTD 172-352) of Kir6.2 and TMD0/L0 (1-284), TMD1 (285-614), NBD1 (615-928), NBD1-TMD2-linker (992-999), TMD2 (1000-1319) and NBD2 (1320-1582) of SUR1. The model containing Aekatperone was then built manually using *Coot*. The resulting model was further refined using *Coot* and *Phenix* iteratively until the statistics and fitting were satisfactory (Table S2, Supplementary Fig. 6C). All cryoEM structure figures were produced with UCSF Chimera, ChimeraX, and PyMol (http://www.pymol.org). Pore radius calculations were performed with HOLE implemented in *Coot*.

Molecular dynamics simulations

We used Gromacs 2023 for MD simulations, based on the Aekatperone-bound K_{ATP} structural model with intrinsically disordered regions reconstructed as in our previous work (Walczewska-Szewc & Nowak, 2023). The system, containing four Kir6.2 and one SUR1, was embedded in a 1-palmitoyl-2-oleoyl-phosphatidylcholine (POPC) lipid bilayer with water (TIP3) and 0.2 M KCl using CHARMM-GUI (Jo et al., 2008; Wu et al., 2014). We applied the CHARMM36m force field for the whole system (Huang et al., 2017). A Swiss param server was used to generate parameters for Aekatperone (Bugnon et al., 2023; Zoete et al., 2011). Short-range Coulomb and van der Waals interactions had 1.0 nm cut-offs, with long-range electrostatics managed by the particle-mesh Ewald method. Bonds were restrained using LINCS. Schrodinger software predicted pKa values and ligand protonation state (Hess, 2008). Energy minimization used the steepest descent algorithm. A 200 ns NVT equilibration with position restraints on backbone and ligand atoms (fc = 1000 kJ/mol/nm²) allows the solvent to adapt to the pore and relaxed IDRs (Supplementary Fig.8). Five 500 ns production runs were in an NPT ensemble with a velocity-rescale thermostat at 309 K (τ = 0.1 ps) and a Parrinello−Rahman barostat at 1 bar (τ = 2 ps) (Bussi et al., 2007; Parrinello & Rahman, 1981).

The stability of Aekatperone binding was analyzed using custom Python3 scripts based on the MDAnalysis library (Michaud-Agrawal et al., 2011). Trajectories were aligned on helices 11, 12, and 14 of the TMD1 and TMD2 domains of SUR1, which form the Aekatperone binding site. The space sampled by the ligand during the simulation was visualized by tracking the center of mass positions of groups a, b, c, d, and e. This allowed us to assess the binding stability and conformational freedom of the entire ligand and each part separately. Key residues involved in ligand binding were identified based on their frequency of remaining in close contact (within 3.5 Å) with the ligand throughout the simulation. Residues that remained in close contact for at least 30% of the simulation time in at least 3 out of 5 trajectories were included. MD simulation figures were generated using VMD 1.9.3.

Statistics

Data are presented as mean ± SEM. Differences were tested using Student's t-test when comparing two groups or one-way analysis of variance (ANOVA) when comparing three or more groups with Tukey's or Dunnett's *post-hoc* tests for multiple comparisons in Graph-Pad Prism 10 as indicated in figure legends. Differences were assumed to be significant if $p \leq 0.05$.

Data availability

The cryo-EM map has been deposited in the Electron Microscopy Data Bank (EMDB), and the coordinates have been deposited in the PDB under the following accession numbers: EMD-46820 and PDB ID 9DFX.

Competing Interests

The authors declare that they have no competing financial or non-financial interests with the contents of this article.

Author contributions

AE designed and performed experiments, prepared figures, and wrote and edited the manuscript. CMD performed cryoEM experiments, analyzed data, prepared figures, wrote and edited the manuscript. HHT performed virtual screening and edited the manuscript. ZY and JA performed experiments. NH oversaw the virtual screening study and read the manuscript. KWS performed MD simulations, analyzed MD simulation data, prepared figures, and edited the manuscript. SLS

conceived the project, performed electrophysiology experiments, prepared figures, wrote and edited the manuscript.

Acknowledgements
A portion of this research was supported by NIH grant U24GM129547 and performed at the Pacific Northwest Cryo-EM Center (PNCC) at Oregon Health and Science University and accessed through EMSL (grid.436923.9), a DOE Office of Science User Facility sponsored by the Office of Biological and Environmental Research, with special thanks to Dr. Nancy Meyer for help with cryoEM data collection. We acknowledge support by the National Institutes of Health grant R01GM145784 (to SLS) and the Egyptian government predoctoral scholarship GM 1109 (to AE). We are grateful to Dr. Bruce L. Patton and Dr. Yi-Ying Kuo for helpful discussions and comments on the manuscript.

References

Aguilar-Bryan, L., & Bryan, J. (1999). Molecular biology of adenosine triphosphate-sensitive potassium channels. *Endocrine reviews*, *20*(2), 101-135.

Ambrósio, A. F., Silva, A. P., Malva, J. O., Soares-da-Silva, P., Carvalho, A. P., & Carvalho, C. M. (1999). Carbamazepine inhibits L-type Ca2+ channels in cultured rat hippocampal neurons stimulated with glutamate receptor agonists. *Neuropharmacology*, *38*(9), 1349-1359. https://doi.org/10.1016/s0028-3908(99)00058-1

Ashcroft, F. M. (2005). ATP-sensitive potassium channelopathies: focus on insulin secretion. *J Clin Invest*, *115*(8), 2047-2058. https://doi.org/10.1172/jci25495

Ashcroft, F. M. (2023). KATP Channels and the Metabolic Regulation of Insulin Secretion in Health and Disease: The 2022 Banting Medal for Scientific Achievement Award Lecture. *Diabetes*, *72*(6), 693-702. https://doi.org/10.2337/dbi22-0030

Atomwise-AIMS-Program. (2024). AI is a viable alternative to high throughput screening: a 318-target study. *Scientific Reports*, *14*(1), 7526. https://doi.org/10.1038/s41598-024-54655-z

Baell, J. B., & Holloway, G. A. (2010). New substructure filters for removal of pan assay interference compounds (PAINS) from screening libraries and for their exclusion in bioassays. *J Med Chem*, *53*(7), 2719-2740. https://doi.org/10.1021/jm901137j

Bernier, V., Lagacé, M., Bichet, D. G., & Bouvier, M. (2004). Pharmacological chaperones: potential treatment for conformational diseases. *Trends Endocrinol Metab*, *15*(5), 222-228. https://doi.org/10.1016/j.tem.2004.05.003

Bruns, R. F., & Watson, I. A. (2012). Rules for identifying potentially reactive or promiscuous compounds. *J Med Chem*, *55*(22), 9763-9772. https://doi.org/10.1021/jm301008n

Bugnon, M., Goullieux, M., Röhrig, U. F., Perez, M. A. S., Daina, A., Michielin, O., & Zoete, V. (2023). SwissParam 2023: A Modern Web-Based Tool for Efficient Small Molecule Parametrization. *J Chem Inf Model*, *63*(21), 6469-6475. https://doi.org/10.1021/acs.jcim.3c01053

Bussi, G., Donadio, D., & Parrinello, M. (2007). Canonical sampling through velocity rescaling. *J Chem Phys*, *126*(1), 014101. https://doi.org/10.1063/1.2408420

Butina, D. (1999). Unsupervised Data Base Clustering Based on Daylight's Fingerprint and Tanimoto Similarity: A Fast and Automated Way To Cluster Small and Large Data Sets. *Journal of Chemical Information and Computer Sciences*, *39*(4), 747-750. https://doi.org/10.1021/ci9803381

Cao, C., Kang, H. J., Singh, I., Chen, H., Zhang, C., Ye, W., Hayes, B. W., Liu, J., Gumpper, R. H., Bender, B. J., Slocum, S. T., Krumm, B. E., Lansu, K., McCorvy, J. D., Kroeze, W. K., English, J. G., DiBerto, J. F., Olsen, R. H. J., Huang, X. P., Zhang, S., Liu, Y., Kim, K., Karpiak, J., Jan, L. Y., Abraham, S. N., Jin, J., Shoichet, B. K., Fay, J. F., & Roth, B. L.

(2021). Structure, function and pharmacology of human itch GPCRs. *Nature*, *600*(7887), 170-175. https://doi.org/10.1038/s41586-021-04126-6

Cartier, E. A., Conti, L. R., Vandenberg, C. A., & Shyng, S. L. (2001). Defective trafficking and function of KATP channels caused by a sulfonylurea receptor 1 mutation associated with persistent hyperinsulinemic hypoglycemia of infancy. *Proc Natl Acad Sci U S A*, *98*(5), 2882-2887. https://doi.org/10.1073/pnas.051499698

Chen, P. C., Olson, E. M., Zhou, Q., Kryukova, Y., Sampson, H. M., Thomas, D. Y., & Shyng, S. L. (2013). Carbamazepine as a novel small molecule corrector of trafficking-impaired ATP-sensitive potassium channels identified in congenital hyperinsulinism. *J Biol Chem*, *288*(29), 20942-20954. https://doi.org/10.1074/jbc.M113.470948

Convertino, M., Das, J., & Dokholyan, N. V. (2016). Pharmacological Chaperones: Design and Development of New Therapeutic Strategies for the Treatment of Conformational Diseases. *ACS Chem Biol*, *11*(6), 1471-1489. https://doi.org/10.1021/acschembio.6b00195

Crane, A., & Aguilar-Bryan, L. (2004). Assembly, maturation, and turnover of K(ATP) channel subunits. *J Biol Chem*, *279*(10), 9080-9090. https://doi.org/10.1074/jbc.M311079200

Cutting, G. R. (2015). Cystic fibrosis genetics: from molecular understanding to clinical application. *Nat Rev Genet*, *16*(1), 45-56. https://doi.org/10.1038/nrg3849

Dabrowski, M., Wahl, P., Holmes, W. E., & Ashcroft, F. M. (2001). Effect of repaglinide on cloned beta cell, cardiac and smooth muscle types of ATP-sensitive potassium channels. *Diabetologia*, *44*(6), 747-756. https://doi.org/10.1007/s001250051684

De Franco, E., Saint-Martin, C., Brusgaard, K., Knight Johnson, A. E., Aguilar-Bryan, L., Bowman, P., Arnoux, J. B., Larsen, A. R., Sanyoura, M., Greeley, S. A. W., Calzada-León, R., Harman, B., Houghton, J. A. L., Nishimura-Meguro, E., Laver, T. W., Ellard, S., Del Gaudio, D., Christesen, H. T., Bellanné-Chantelot, C., & Flanagan, S. E. (2020). Update of variants identified in the pancreatic β-cell K(ATP) channel genes KCNJ11 and ABCC8 in individuals with congenital hyperinsulinism and diabetes. *Hum Mutat*, *41*(5), 884-905. https://doi.org/10.1002/humu.23995

Devaraneni, P. K., Martin, G. M., Olson, E. M., Zhou, Q., & Shyng, S.-L. (2015). Structurally distinct ligands rescue biogenesis defects of the KATP channel complex via a converging mechanism. *Journal of Biological Chemistry*, *290*(12), 7980-7991.

Ding, D., Wang, M., Wu, J. X., Kang, Y., & Chen, L. (2019). The Structural Basis for the Binding of Repaglinide to the Pancreatic K(ATP) Channel. *Cell Rep*, *27*(6), 1848-1857.e1844. https://doi.org/10.1016/j.celrep.2019.04.050

Driggers, C. M., Kuo, Y. Y., Zhu, P., ElSheikh, A., & Shyng, S. L. (2024). Structure of an open K(ATP) channel reveals tandem PIP(2) binding sites mediating the Kir6.2 and SUR1 regulatory interface. *Nat Commun*, *15*(1), 2502. https://doi.org/10.1038/s41467-024-46751-5

Driggers, C. M., & Shyng, S. L. (2021). Production and purification of ATP-sensitive potassium channel particles for cryo-electron microscopy. *Methods Enzymol*, *653*, 121-150. https://doi.org/10.1016/bs.mie.2021.02.008

Driggers, C. M., & Shyng, S. L. (2023). Mechanistic insights on KATP channel regulation from cryo-EM structures. *J Gen Physiol*, *155*(1). https://doi.org/10.1085/jgp.202113046

ElSheikh, A., Driggers, C. M., & Shyng, S.-L. (2024). Non-radioactive Rb+ Efflux Assay for Screening KATP Channel Modulators. In S. Furini (Ed.), *Potassium Channels: Methods and Protocols* (pp. 191-210). Springer US. https://doi.org/10.1007/978-1-0716-3818-7_12

ElSheikh, A., & Shyng, S. L. (2023). K(ATP) channel mutations in congenital hyperinsulinism: Progress and challenges towards mechanism-based therapies. *Front Endocrinol (Lausanne)*, *14*, 1161117. https://doi.org/10.3389/fendo.2023.1161117

Fink, E. A., Xu, J., Hübner, H., Braz, J. M., Seemann, P., Avet, C., Craik, V., Weikert, D., Schmidt, M. F., Webb, C. M., Tolmachova, N. A., Moroz, Y. S., Huang, X. P., Kalyanaraman, C., Gahbauer, S., Chen, G., Liu, Z., Jacobson, M. P., Irwin, J. J., Bouvier, M., Du, Y., Shoichet, B. K., Basbaum, A. I., & Gmeiner, P. (2022). Structure-based discovery of nonopioid analgesics acting through the α(2A)-adrenergic receptor. *Science*, *377*(6614), eabn7065. https://doi.org/10.1126/science.abn7065

Fukuda, Y., Aguilar-Bryan, L., Vaxillaire, M., Dechaume, A., Wang, Y., Dean, M., Moitra, K., Bryan, J., & Schuetz, J. D. (2011). Conserved intramolecular disulfide bond is critical to trafficking and fate of ATP-binding cassette (ABC) transporters ABCB6 and sulfonylurea receptor 1 (SUR1)/ABCC8. *J Biol Chem*, *286*(10), 8481-8492. https://doi.org/10.1074/jbc.M110.174516

Gambeta, E., Chichorro, J. G., & Zamponi, G. W. (2020). Trigeminal neuralgia: An overview from pathophysiology to pharmacological treatments. *Mol Pain*, *16*, 1744806920901890. https://doi.org/10.1177/1744806920901890

Gniewek, P., Worley, B., Stafford, K., Bedem, H. v. d., & Anderson, B. (2021). Learning physics confers pose-sensitivity in structure-based virtual screening. *arXiv preprint arXiv:2110.15459*.

Grotsch, K., Sadybekov, A. V., Hiller, S., Zaidi, S., Eremin, D., Le, A., Liu, Y., Smith, E. C., Illiopoulis-Tsoutsouvas, C., Thomas, J., Aggarwal, S., Pickett, J. E., Reyes, C., Picazo, E., Roth, B. L., Makriyannis, A., Katritch, V., & Fokin, V. V. (2024). Virtual Screening of a Chemically Diverse "Superscaffold" Library Enables Ligand Discovery for a Key GPCR Target. *ACS Chem Biol*, *19*(4), 866-874. https://doi.org/10.1021/acschembio.3c00602

Hess, B. (2008). P-LINCS: A Parallel Linear Constraint Solver for Molecular Simulation. *J Chem Theory Comput*, *4*(1), 116-122. https://doi.org/10.1021/ct700200b

Hewat, T. I., Johnson, M. B., & Flanagan, S. E. (2022). Congenital Hyperinsulinism: Current Laboratory-Based Approaches to the Genetic Diagnosis of a Heterogeneous Disease. *Front Endocrinol (Lausanne)*, *13*, 873254. https://doi.org/10.3389/fendo.2022.873254

Hohmeier, H. E., Mulder, H., Chen, G., Henkel-Rieger, R., Prentki, M., & Newgard, C. B. (2000). Isolation of INS-1-derived cell lines with robust ATP-sensitive K+ channel-dependent and -independent glucose-stimulated insulin secretion. *Diabetes*, *49*(3), 424-430. https://doi.org/10.2337/diabetes.49.3.424

Huang, J., Rauscher, S., Nawrocki, G., Ran, T., Feig, M., de Groot, B. L., Grubmüller, H., & MacKerell, A. D., Jr. (2017). CHARMM36m: an improved force field for folded and intrinsically disordered proteins. *Nat Methods*, *14*(1), 71-73. https://doi.org/10.1038/nmeth.4067

Jo, S., Kim, T., Iyer, V. G., & Im, W. (2008). CHARMM-GUI: a web-based graphical user interface for CHARMM. *J Comput Chem*, *29*(11), 1859-1865. https://doi.org/10.1002/jcc.20945

Kharade, S. V., Nichols, C., & Denton, J. S. (2016). The shifting landscape of KATP channelopathies and the need for 'sharper' therapeutics. *Future Med Chem*, *8*(7), 789-802. https://doi.org/10.4155/fmc-2016-0005

Lee, K. P. K., Chen, J., & MacKinnon, R. (2017). Molecular structure of human KATP in complex with ATP and ADP. *Elife*, *6*. https://doi.org/10.7554/eLife.32481

Leidenheimer, N. J., & Ryder, K. G. (2014). Pharmacological chaperoning: a primer on mechanism and pharmacology. *Pharmacol Res*, *83*, 10-19. https://doi.org/10.1016/j.phrs.2014.01.005

Lin, C. W., Yan, F., Shimamura, S., Barg, S., & Shyng, S. L. (2005). Membrane phosphoinositides control insulin secretion through their effects on ATP-sensitive K+ channel activity. *Diabetes*, *54*(10), 2852-2858. https://doi.org/10.2337/diabetes.54.10.2852

Lin, Y. W., Bushman, J. D., Yan, F. F., Haidar, S., MacMullen, C., Ganguly, A., Stanley, C. A., & Shyng, S. L. (2008). Destabilization of ATP-sensitive potassium channel activity by novel KCNJ11 mutations identified in congenital hyperinsulinism. *J Biol Chem*, *283*(14), 9146-9156. https://doi.org/10.1074/jbc.M708798200

Liu, F., Kaplan, A. L., Levring, J., Einsiedel, J., Tiedt, S., Distler, K., Omattage, N. S., Kondratov, I. S., Moroz, Y. S., Pietz, H. L., Irwin, J. J., Gmeiner, P., Shoichet, B. K., & Chen, J. (2024). Structure-based discovery of CFTR potentiators and inhibitors. *Cell*, *187*(14), 3712-3725.e3734. https://doi.org/10.1016/j.cell.2024.04.046

Martin, G. M., Kandasamy, B., DiMaio, F., Yoshioka, C., & Shyng, S. L. (2017). Anti-diabetic drug binding site in a mammalian KATP channel revealed by Cryo-EM. *Elife*, *6*. https://doi.org/10.7554/eLife.31054

Martin, G. M., Rex, E. A., Devaraneni, P., Denton, J. S., Boodhansingh, K. E., DeLeon, D. D., Stanley, C. A., & Shyng, S. L. (2016). Pharmacological Correction of Trafficking Defects in ATP-sensitive Potassium Channels Caused by Sulfonylurea Receptor 1 Mutations. *J Biol Chem*, *291*(42), 21971-21983. https://doi.org/10.1074/jbc.M116.749366

Martin, G. M., Sung, M. W., & Shyng, S. L. (2020). Pharmacological chaperones of ATP-sensitive potassium channels: Mechanistic insight from cryoEM structures. *Mol Cell Endocrinol*, *502*, 110667. https://doi.org/10.1016/j.mce.2019.110667

Martin, G. M., Sung, M. W., Yang, Z., Innes, L. M., Kandasamy, B., David, L. L., Yoshioka, C., & Shyng, S. L. (2019). Mechanism of pharmacochaperoning in a mammalian KATP channel revealed by cryo-EM. *Elife*, *8*. https://doi.org/10.7554/eLife.46417

Martin, G. M., Yoshioka, C., Rex, E. A., Fay, J. F., Xie, Q., Whorton, M. R., Chen, J. Z., & Shyng, S. L. (2017). Cryo-EM structure of the ATP-sensitive potassium channel illuminates mechanisms of assembly and gating. *Elife*, *6*. https://doi.org/10.7554/eLife.24149

Matsumoto, A., Arisaka, H., Hosokawa, Y., Sakuraba, S., Sugita, T., Umezawa, N., Kaku, Y., Yoshida, K., & Kuwana, S. (2015). Effect of carbamazepine and gabapentin on excitability in the trigeminal subnucleus caudalis of neonatal rats using a voltage-sensitive dye imaging technique. *Biol Res*, *48*(1), 36. https://doi.org/10.1186/s40659-015-0027-6

Merrins, M. J., Corkey, B. E., Kibbey, R. G., & Prentki, M. (2022). Metabolic cycles and signals for insulin secretion. *Cell Metab*, *34*(7), 947-968. https://doi.org/10.1016/j.cmet.2022.06.003

Michaud-Agrawal, N., Denning, E. J., Woolf, T. B., & Beckstein, O. (2011). MDAnalysis: a toolkit for the analysis of molecular dynamics simulations. *J Comput Chem*, *32*(10), 2319-2327. https://doi.org/10.1002/jcc.21787

Nichols, C. G. (2006). KATP channels as molecular sensors of cellular metabolism. *Nature*, *440*(7083), 470-476. https://doi.org/10.1038/nature04711

Nichols, C. G. (2023). Personalized Therapeutics for K(ATP)-Dependent Pathologies. *Annu Rev Pharmacol Toxicol*, *63*, 541-563. https://doi.org/10.1146/annurev-pharmtox-051921-123023

Nichols, C. G., Shyng, S. L., Nestorowicz, A., Glaser, B., Clement, J. P. t., Gonzalez, G., Aguilar-Bryan, L., Permutt, M. A., & Bryan, J. (1996). Adenosine diphosphate as an intracellular regulator of insulin secretion. *Science*, *272*(5269), 1785-1787. https://doi.org/10.1126/science.272.5269.1785

Nichols, C. G., York, N. W., & Remedi, M. S. (2022). ATP-Sensitive Potassium Channels in Hyperinsulinism and Type 2 Diabetes: Inconvenient Paradox or New Paradigm? *Diabetes*, *71*(3), 367-375. https://doi.org/10.2337/db21-0755

Parrinello, M., & Rahman, A. (1981). Polymorphic transitions in single crystals: A new molecular dynamics method. *Journal of Applied Physics*, *52*(12), 7182-7190. https://doi.org/10.1063/1.328693

Pipatpolkai, T., Usher, S., Stansfeld, P. J., & Ashcroft, F. M. (2020). New insights into K(ATP) channel gene mutations and neonatal diabetes mellitus. *Nat Rev Endocrinol*, *16*(7), 378-393. https://doi.org/10.1038/s41574-020-0351-y

Punjani, A., Rubinstein, J. L., Fleet, D. J., & Brubaker, M. A. (2017). cryoSPARC: algorithms for rapid unsupervised cryo-EM structure determination. *Nat Methods*, *14*(3), 290-296. https://doi.org/10.1038/nmeth.4169

Quast, U., Stephan, D., Bieger, S., & Russ, U. (2004). The impact of ATP-sensitive K+ channel subtype selectivity of insulin secretagogues for the coronary vasculature and the myocardium. *Diabetes*, *53 Suppl 3*, S156-164. https://doi.org/10.2337/diabetes.53.suppl_3.s156

Raab-Graham, K. F., Cirilo, L. J., Boettcher, A. A., Radeke, C. M., & Vandenberg, C. A. (1999). Membrane topology of the amino-terminal region of the sulfonylurea receptor. *J Biol Chem*, *274*(41), 29122-29129. https://doi.org/10.1074/jbc.274.41.29122

Reimann, F., Proks, P., & Ashcroft, F. M. (2001). Effects of mitiglinide (S 21403) on Kir6.2/SUR1, Kir6.2/SUR2A and Kir6.2/SUR2B types of ATP-sensitive potassium channel. *Br J Pharmacol*, *132*(7), 1542-1548. https://doi.org/10.1038/sj.bjp.0703962

Rosenfeld, E., Ganguly, A., & De Leon, D. D. (2019). Congenital hyperinsulinism disorders: Genetic and clinical characteristics. *Am J Med Genet C Semin Med Genet*, *181*(4), 682-692. https://doi.org/10.1002/ajmg.c.31737

Rosenthal, P. B., & Henderson, R. (2003). Optimal Determination of Particle Orientation, Absolute Hand, and Contrast Loss in Single-particle Electron Cryomicroscopy. *Journal of Molecular Biology*, *333*(4), 721-745. https://doi.org/https://doi.org/10.1016/j.jmb.2003.07.013

Sahin, I., Bakiner, O., Demir, T., Sari, R., & Atmaca, A. (2024). Current Position of Gliclazide and Sulfonylureas in the Contemporary Treatment Paradigm for Type 2 Diabetes: A Scoping Review. *Diabetes Ther*, *15*(8), 1687-1716. https://doi.org/10.1007/s13300-024-01612-8

Schwartz, T. B., & Meinert, C. L. (2004). The UGDP controversy: thirty-four years of contentious ambiguity laid to rest. *Perspect Biol Med*, *47*(4), 564-574. https://doi.org/10.1353/pbm.2004.0071

Shyng, S. L. (2022). K(ATP) Channel Function: More than Meets the Eye. *Function (Oxf)*, *3*(1), zqab070. https://doi.org/10.1093/function/zqab070

Shyng, S. L., Ferrigni, T., Shepard, J. B., Nestorowicz, A., Glaser, B., Permutt, M. A., & Nichols, C. G. (1998). Functional analyses of novel mutations in the sulfonylurea receptor 1 associated with persistent hyperinsulinemic hypoglycemia of infancy. *Diabetes*, *47*(7), 1145-1151. https://doi.org/10.2337/diabetes.47.7.1145

Shyng, S. L., & Nichols, C. G. (1998). Membrane phospholipid control of nucleotide sensitivity of KATP channels. *Science*, *282*(5391), 1138-1141. http://www.ncbi.nlm.nih.gov/htbin-post/Entrez/query?db=m&form=6&dopt=r&uid=9804554

Stafford, K. A., Anderson, B. M., Sorenson, J., & Van Den Bedem, H. (2022). AtomNet PoseRanker: Enriching ligand pose quality for dynamic proteins in virtual high-throughput screens. *Journal of Chemical Information and Modeling*, *62*(5), 1178-1189.

Stanley, C. A. (2016). Perspective on the Genetics and Diagnosis of Congenital Hyperinsulinism Disorders. *J Clin Endocrinol Metab*, *101*(3), 815-826. https://doi.org/10.1210/jc.2015-3651

Sung, M. W., Driggers, C. M., Mostofian, B., Russo, J. D., Patton, B. L., Zuckerman, D. M., & Shyng, S. L. (2022). Ligand-mediated Structural Dynamics of a Mammalian Pancreatic K(ATP) Channel. *J Mol Biol*, *434*(19), 167789. https://doi.org/10.1016/j.jmb.2022.167789

Thompson, B., & Satin, L. S. (2021). Beta-Cell Ion Channels and Their Role in Regulating Insulin Secretion. *Compr Physiol*, *11*(4), 1-21. https://doi.org/10.1002/cphy.c210004

Tikhonov, D. B., & Zhorov, B. S. (2017). Mechanism of sodium channel block by local anesthetics, antiarrhythmics, and anticonvulsants. *J Gen Physiol*, *149*(4), 465-481. https://doi.org/10.1085/jgp.201611668

Walczewska-Szewc, K., & Nowak, W. (2023). Structural Insights into ATP-Sensitive Potassium Channel Mechanics: A Role of Intrinsically Disordered Regions. *J Chem Inf Model*, *63*(6), 1806-1818. https://doi.org/10.1021/acs.jcim.2c01196

Wallach, I., Dzamba, M., & Heifets, A. (2015). AtomNet: a deep convolutional neural network for bioactivity prediction in structure-based drug discovery. *arXiv preprint arXiv:1510.02855*.

Wang, M., Wu, J. X., & Chen, L. (2022). Structural Insights Into the High Selectivity of the Anti-Diabetic Drug Mitiglinide. *Front Pharmacol*, *13*, 929684. https://doi.org/10.3389/fphar.2022.929684

Wu, E. L., Cheng, X., Jo, S., Rui, H., Song, K. C., Dávila-Contreras, E. M., Qi, Y., Lee, J., Monje-Galvan, V., Venable, R. M., Klauda, J. B., & Im, W. (2014). CHARMM-GUI Membrane Builder toward realistic biological membrane simulations. *J Comput Chem*, *35*(27), 1997-2004. https://doi.org/10.1002/jcc.23702

Wu, J. X., Ding, D., Wang, M., & Chen, L. (2020). Structural Insights into the Inhibitory Mechanism of Insulin Secretagogues on the Pancreatic ATP-Sensitive Potassium Channel. *Biochemistry*, *59*(1), 18-25. https://doi.org/10.1021/acs.biochem.9b00692

Wu, J. X., Ding, D., Wang, M., Kang, Y., Zeng, X., & Chen, L. (2018). Ligand binding and conformational changes of SUR1 subunit in pancreatic ATP-sensitive potassium channels. *Protein Cell*, *9*(6), 553-567. https://doi.org/10.1007/s13238-018-0530-y

Yan, F., Lin, C. W., Weisiger, E., Cartier, E. A., Taschenberger, G., & Shyng, S. L. (2004). Sulfonylureas correct trafficking defects of ATP-sensitive potassium channels caused by mutations in the sulfonylurea receptor. *J Biol Chem*, *279*(12), 11096-11105. https://doi.org/10.1074/jbc.M312810200

Yan, F. F., Casey, J., & Shyng, S. L. (2006). Sulfonylureas correct trafficking defects of disease-causing ATP-sensitive potassium channels by binding to the channel complex. *J Biol Chem*, *281*(44), 33403-33413. https://doi.org/10.1074/jbc.M605195200

Yan, F. F., Lin, Y. W., MacMullen, C., Ganguly, A., Stanley, C. A., & Shyng, S. L. (2007). Congenital hyperinsulinism associated ABCC8 mutations that cause defective trafficking of ATP-sensitive K+ channels: identification and rescue. *Diabetes*, *56*(9), 2339-2348. https://doi.org/10.2337/db07-0150

Zerangue, N., Schwappach, B., Jan, Y. N., & Jan, L. Y. (1999). A new ER trafficking signal regulates the subunit stoichiometry of plasma membrane KATP channels. *Neuron*, *22*(3), 537-548.

Zhao, C., & MacKinnon, R. (2021). Molecular structure of an open human K(ATP) channel. *Proc Natl Acad Sci U S A*, *118*(48). https://doi.org/10.1073/pnas.2112267118

Zoete, V., Cuendet, M. A., Grosdidier, A., & Michielin, O. (2011). SwissParam: a fast force field generation tool for small organic molecules. *J Comput Chem*, *32*(11), 2359-2368. https://doi.org/10.1002/jcc.21816

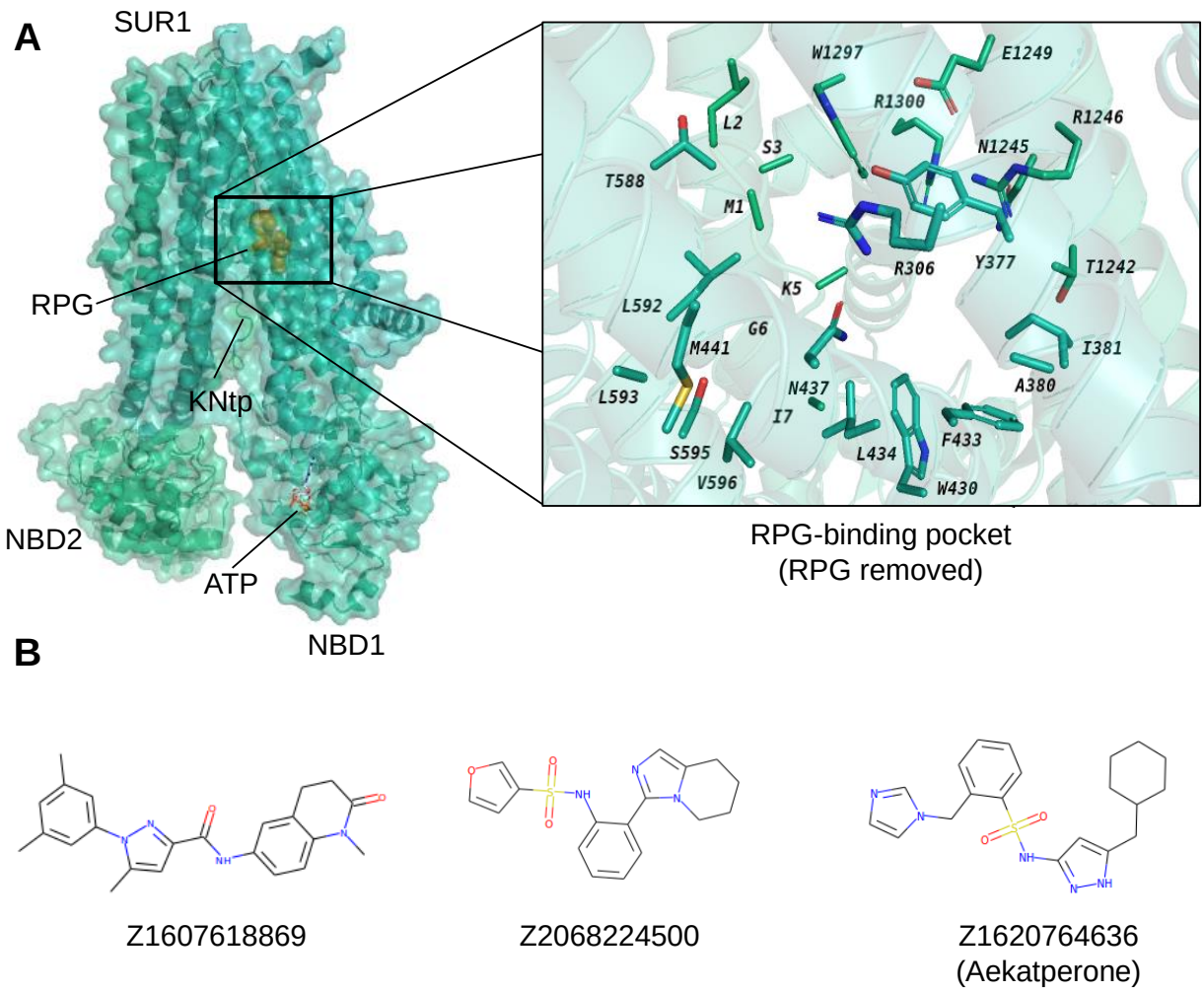

Figure 1. Identification of potential pharmacochaperones for pancreatic K_{ATP} channels through virtual screening and experimental validation. (A) *Left*: CryoEM structure of repaglinide (RPG)-bound pancreatic K_{ATP} channel (PDB ID: 6PZ9; only the SUR1 ABC core and Kir6.2-N terminal peptide are shown; RPG is shown in gold spheres and ATP bound at the NBD1 of SUR1 is shown as red sticks). *Right*: a close-up view of the target site used for virtual screening of a library of ~2.5 million compounds (from Enamine), utilizing the AtomNet model (RPG is removed to show only the binding residues from SUR1). From this screening, a set of 96 “top scoring compounds" was selected for experimental validation. (**B**) Chemical structures of the top three compounds, C24, C27, and C45, identified via experimental testing of pharmacochaperone effects on a K_{ATP} trafficking mutant (**Supplementary Fig. 1**) correspond to ZINC IDs Z1607618869, Z2068224500, and Z1620764636 respectively.

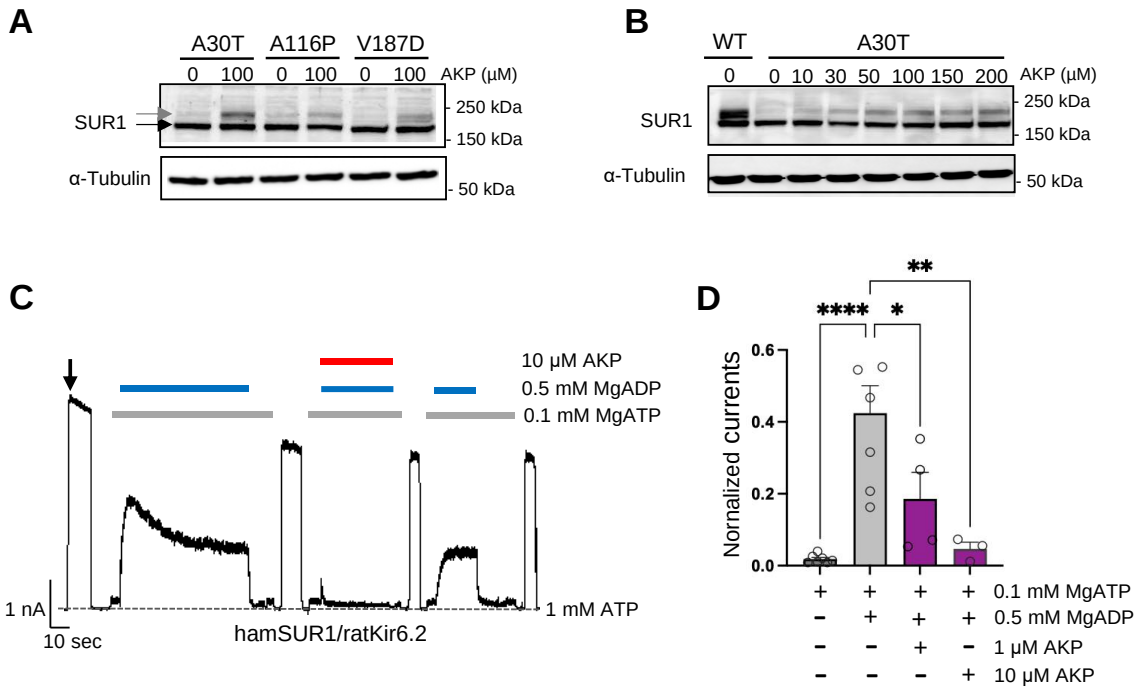

Figure 2. Aekatperone has dual pharmacochaperone and inhibitory actions on pancreatic K_{ATP} channels. (A) Representative western blots of SUR1 from COSm6 cells co-transfected with cDNAs of WT Kir6.2 and trafficking mutants of SUR1 TMD0 domain, A30T, A116P or V187D, and treated with either 0.1% DMSO (0 μM) or 100 μM Aekatperone (AKP) for 16 hours. The core-glycosylated immature SUR1 and the complex-glycosylated mature SUR1 are indicated by the black and grey arrows, respectively. The tubulin blot below serves as a loading control. **(B)** Representative western blots of SUR1 from COSm6 cells co-transfected with cDNAs of WT Kir6.2 and a SUR1 trafficking mutant A30T, and treated with either 0.1% DMSO (0 μM) or various concentrations of Aekatperone (10, 50, 100, 150, 200 μM) for 16 hours. WT SUR1 from cells co-transfected with WT Kir6.2 and WT SUR1 without Aekatperone treatment served as a control (left lane). **(C)** Representative recording from COSm6 cells co-transfected with hamster SUR1 and rat Kir6.2. Channels were exposed to K-INT solution upon patch excision (arrow) and exposed to solutions containing MgATP, MgADP, or Aekatperone as indicated by the bars above the recordings and the labels on the right. The patch was exposed to 1mM ATP periodically to ensure the baseline has not shifted (grey dashed line). **(D)** Quantification of currents (normalized to currents in K-INT/1 mM EDTA at the time of patch excision) in various solutions from recordings such as that shown in (A). Each bar represents the mean ± SEM of at least 3 patches, with circles showing individual patches. *$p < 0.05$ by one-way ANOVA and Dunnet's *post-hoc* test.

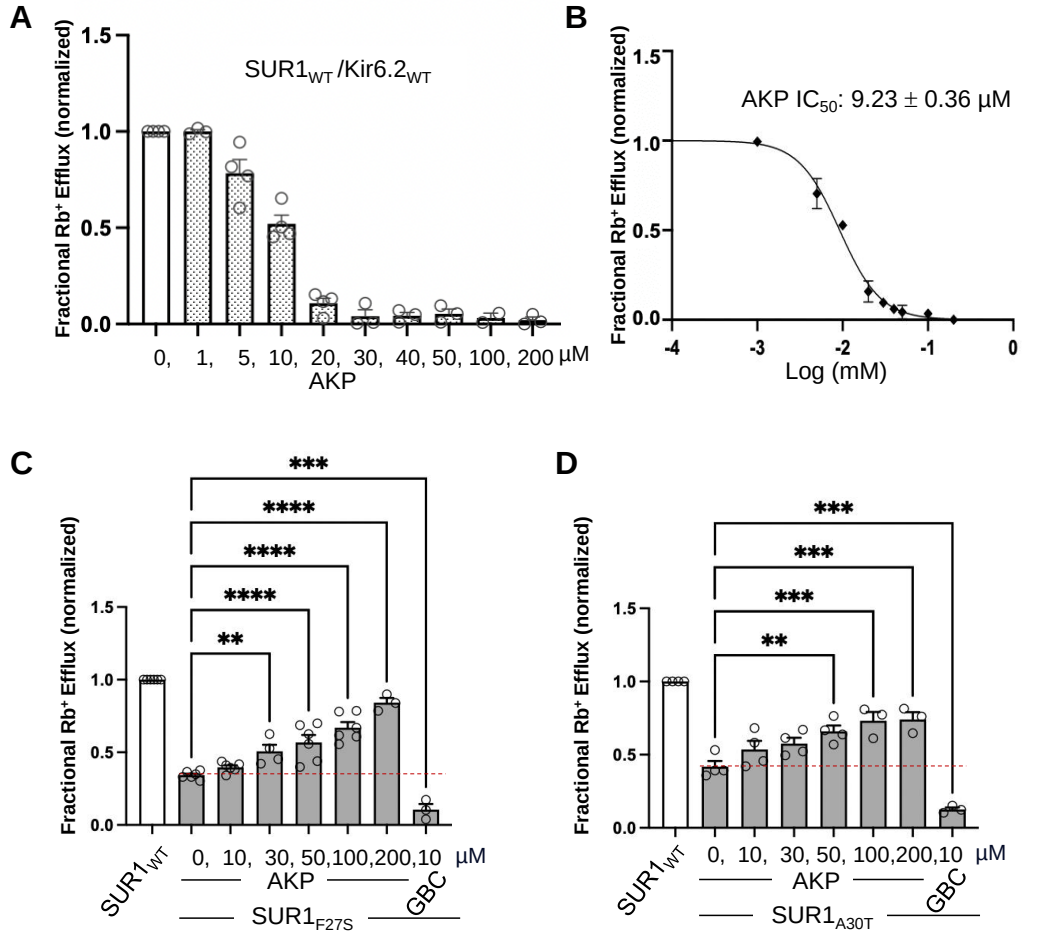

Figure 3. Functional recovery of mutant K_{ATP} channels rescued by Aekatperone. (A) Rb^+ efflux assay results showing Aekatperone (AKP) dose-dependently inhibited WT pancreatic K_{ATP} channels (hamster SUR1 and rat Kir6.2) expressed in COSm6 cells and opened by metabolic inhibition (see Methods). The fractional Rb^+ efflux was calculated by subtracting efflux in untransfected cells and normalizing to efflux in cells treated with 0.1% DMSO. **(B)** Dose-response curve of Aekatperone inhibition from data shown in (A) fitted with a Hill equation with variable slope using GraphPad Prism 10. The IC_{50} is 9.23 µM ± 0.36 µM. Error bars represent the SEM. **(C, D)** Bar graphs showing dose-response enhancement in K_{ATP} channel activity as assessed by Rb^+ efflux assay in COSm6 cells expressing two different trafficking mutations, $SUR1_{F27S}$ (A) and $SUR1_{A30T}$ (B). The cells were treated with varying concentrations of Aekatperone (10, 30, 50, 100, or 200 µM), GBC at 10 µM, or 0.1% DMSO as a vehicle control (0 µM Aekatperone) for 16 hours. Aekatperone and GBC was excluded from the efflux solutions during the efflux assay. Untransfected (UT) cells were included to quantify background Rb^+ efflux, which was subtracted from other experimental readings. The data were normalized to the fractional Rb^+ efflux of cells expressing WT channels. Error bars represent the SEM of at least 3 independent experiments (circles are individual data points from 3-6 different experiments). Statistical significance was performed using one-way ANOVA followed by Dunnett's *post-hoc* multiple comparison test, alpha = 0.05. *p < 0.05, **p< 0.01, ***p< 0.001, ****p< 0.0001. A red dashed line is shown to indicate the basal efflux of the mutant channels under vehicle control conditions (in the absence of Aekatperone). **(E)** Schematic of experimental design for **(F)**. COSm6 cells transfected with WT or various mutant channels were treated with 0.1% DMSO (vehicle control) or 100 Aekatperone (AKP) overnight in the presence of Rb^+. Before efflux measurements, cells were washed in a RbCl containing buffer lacking AKP for 30 min. Efflux was then measured for 30 min in a Ringer's solution ± Diazoxide (Diaz) at 200 µM. Note, diazoxide was included in Ringer's solution during the efflux assay but not during the overnight incubation. **(F)** Rb^+ efflux experiments showing overnight treatment with AKP enhances acute Diaz response in COSm6 cells expressing trafficking mutants. Each bar represents the mean ± SEM of at least 3 different biological repeats, with circles indicating individual data points, alpha = 0.05. *p < 0.05, **p < 0.01, ***p < 0.001, ****p < 0.0001 by one-way ANOVA with Dunnett's multiple comparisons test.

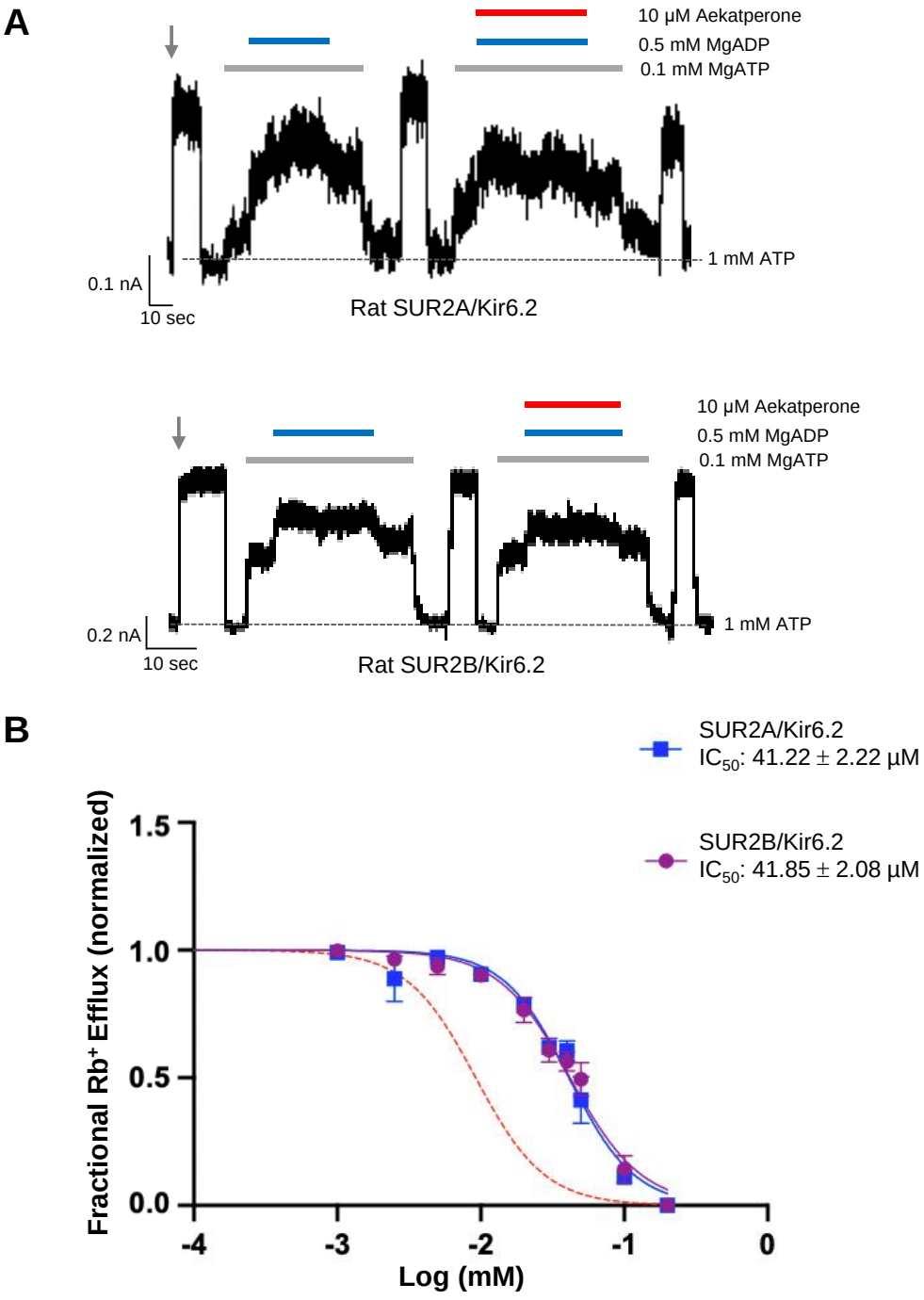

Figure 4. SUR2-containing K_{ATP} channels are less sensitive to Aekatperone inhibitory effects. (A) Representative recordings from COSm6 cells expressing SUR2A/Kir6.2 (top) or SUR2B/Kir6.2 channels. Channels were exposed to K-INT solution upon patch excision (grey arrow) and exposed to solutions containing MgATP, MgADP, or Aekatperone as indicated by the bars above the recordings and the labels on the right. The patch was exposed to 1 mM ATP periodically to ensure the baseline has not shifted (grey dashed line). **(B)** IC_{50} of Aekatperone on SUR2A/Kir6.2 or SUR2B/Kir6.2 channels transiently expressed in COSm6 cells Kir6.2 using Rb^+ efflux assay. Data were fit with a Hill equation with variable slope using GraphPad Prism 10. The Aekatperone IC_{50} is 41.22 μM ± 2.22 μM (SEM) for SUR2A/Kir6.2 channels and 41.85 μM ± 2.08 μM (SEM) for SUR2B/Kir6.2 channels. The error bar for each data point represents the SEM. Red dotted line represents the dose response curve of Aekatperone on SUR1/Kir6.2 channels from Fig.3B for comparison.

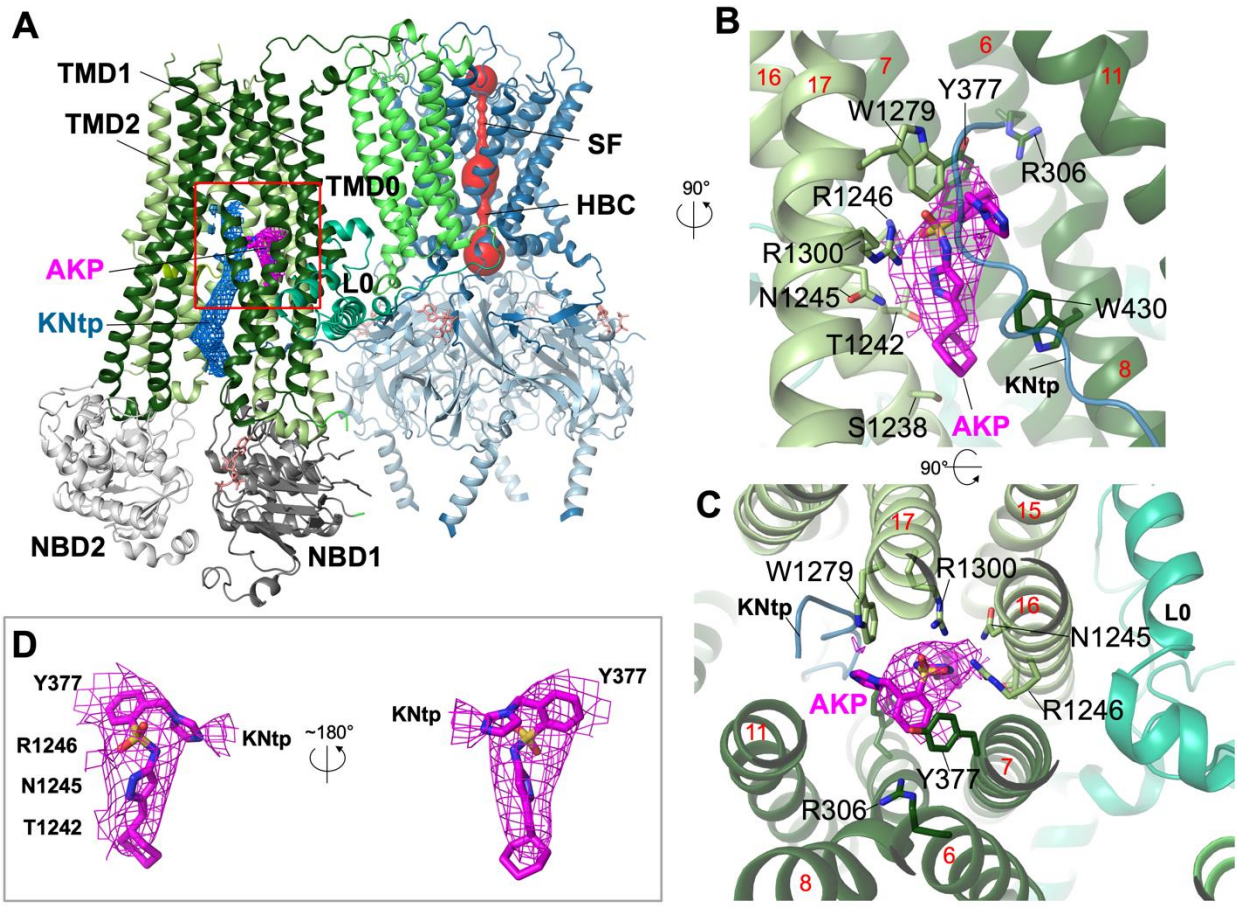

Figure 5. Structure of the K_{ATP} channel in complex with Aekatperone. (A) Structural model of the pancreatic K_{ATP} channel in complex with Aekatperone showing SUR1 in NBD-separated conformation and the Kir6.2 pore (red) constricted at the helical bundle crossing (HBC) and the selectivity filter (SF) gates. Aekatperone is shown as purple mesh (0.08V contour) and N-terminal domain of Kir6.2 (KNtp) as blue mesh (0.08 V contour). Only one SUR1 subunit attached to Kir6.2 core is shown based on the focused refinement cryoEM map of the Kir6.2 tetramer and a single SUR1 subunit. SUR1 transmembrane domain (TMD) 1 and 2 are colored in dark green and light green, respectively. NBD; Nucleotide binding domain, L0; L0 loop of SUR1. **(B, C)** Close-up sideview (B) and top down view of the Aekatperone binding site. Aekatperone cryoEM density and model are shown in magenta and SUR1 residues that interact with Aekatperone are shown as sticks. KNtp is shown as a blue main chain peptide. Red numbers indicate the numbers of helices of SUR1. **(D)** Aekatperone cryoEM density map (0.08 V contour) and model fitting in two different views. Note at the contour shown, some surrounding density from interacting SUR1 and Kir6.2 is included.

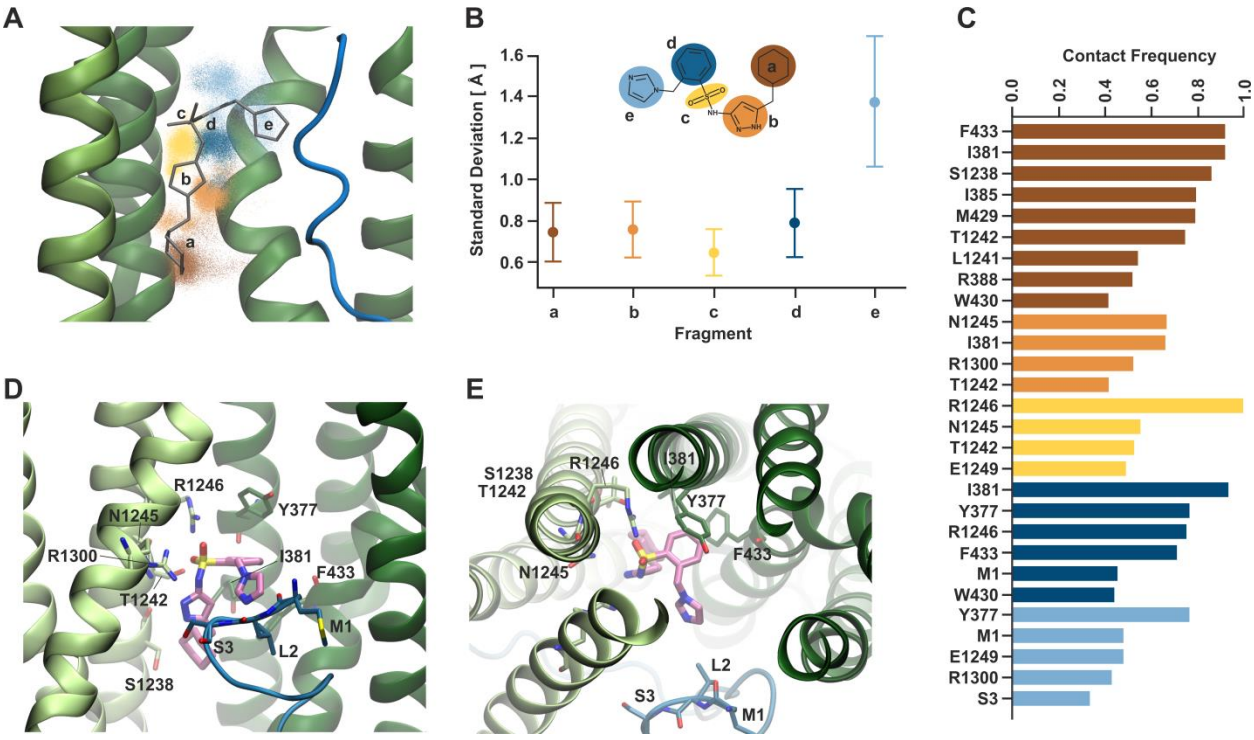

Figure 6. Dynamical behavior of Aekatperone in the SUR1 cavity investigated by molecular dynamics (MD) simulations. (A) Scatter of the positions of the centers of mass of individual fragments of Aekatperone during the simulation. The initial position is marked as sticks. Light green helices belong to TMD2, dark green to TMD1, and the blue fragment is KNtp. **(B)** Standard deviation of the positions of the centers of mass of individual fragments during the simulation. The fragments are color-coded throughout the figure. **(C)** Frequency of staying in close contact with SUR1 and KNtp residues during the simulation, divided by individual fragments. **(D, E)** An example snapshot from the simulation of Aekatperone in the pocket showing its interactions with SUR1 and KNtp residues - side view (D) and top view (E).

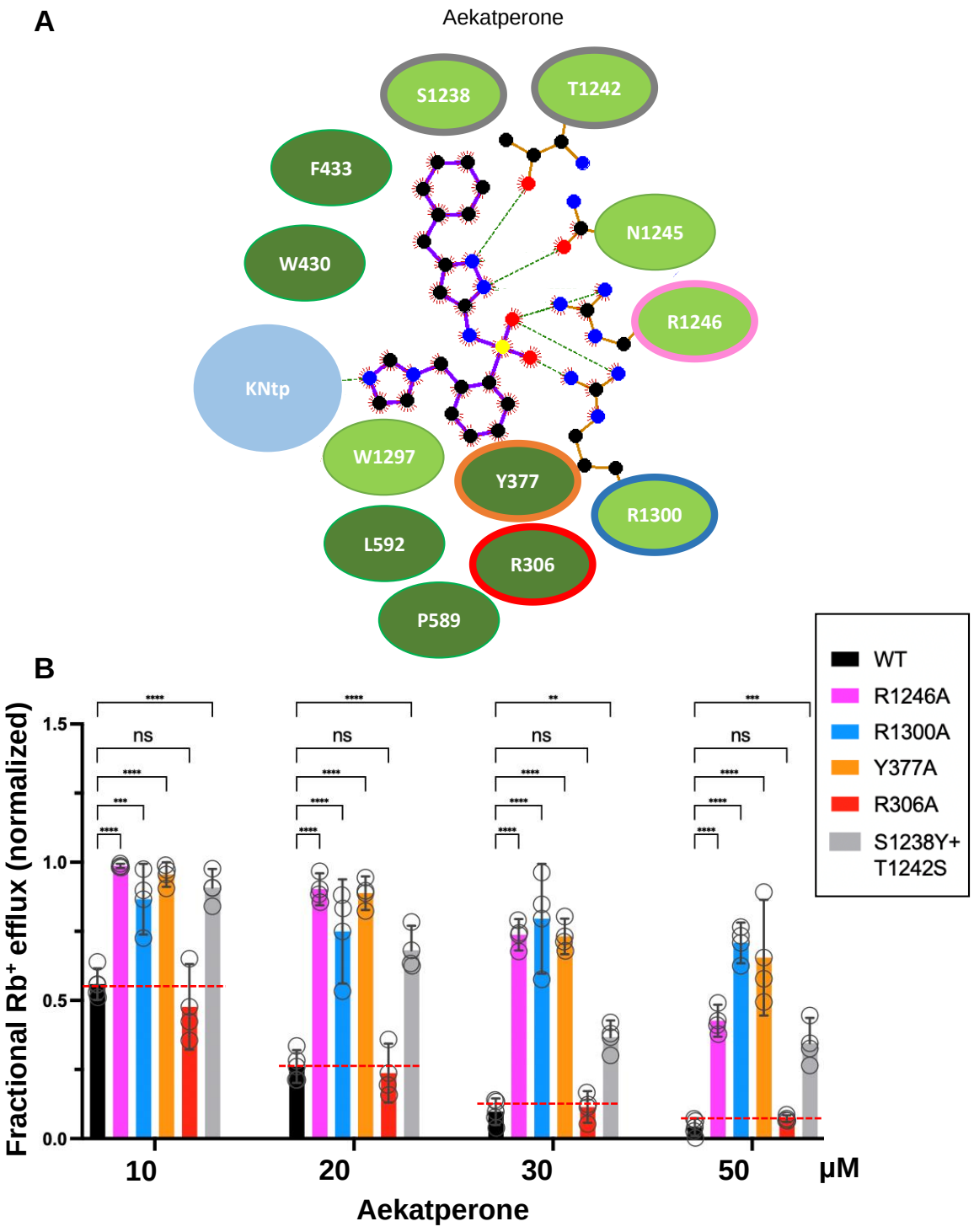

Figure 7. Mutagenesis studies supporting the Aekatperone binding site model derived from Cryo-EM. (A) 2D Aekatperone binding site model showing chemical interactions between the compound and surrounding SUR1 residues and KNtp. **(B)** Rb^+ efflux experiments testing the effect of mutating select binding site residues on channel response to Aekatperone. Each bar is the mean and error bars represent the SEM of 3 independent experiments (individual data points shown as circles). Statistical significance is based on two-way ANOVA with Dunnett's *post-hoc* multiple comparisons test, with alpha = 0.05. $^{**}p < 0.01$, $^{***}p < 0.001$, $^{****}p < 0.0001$.

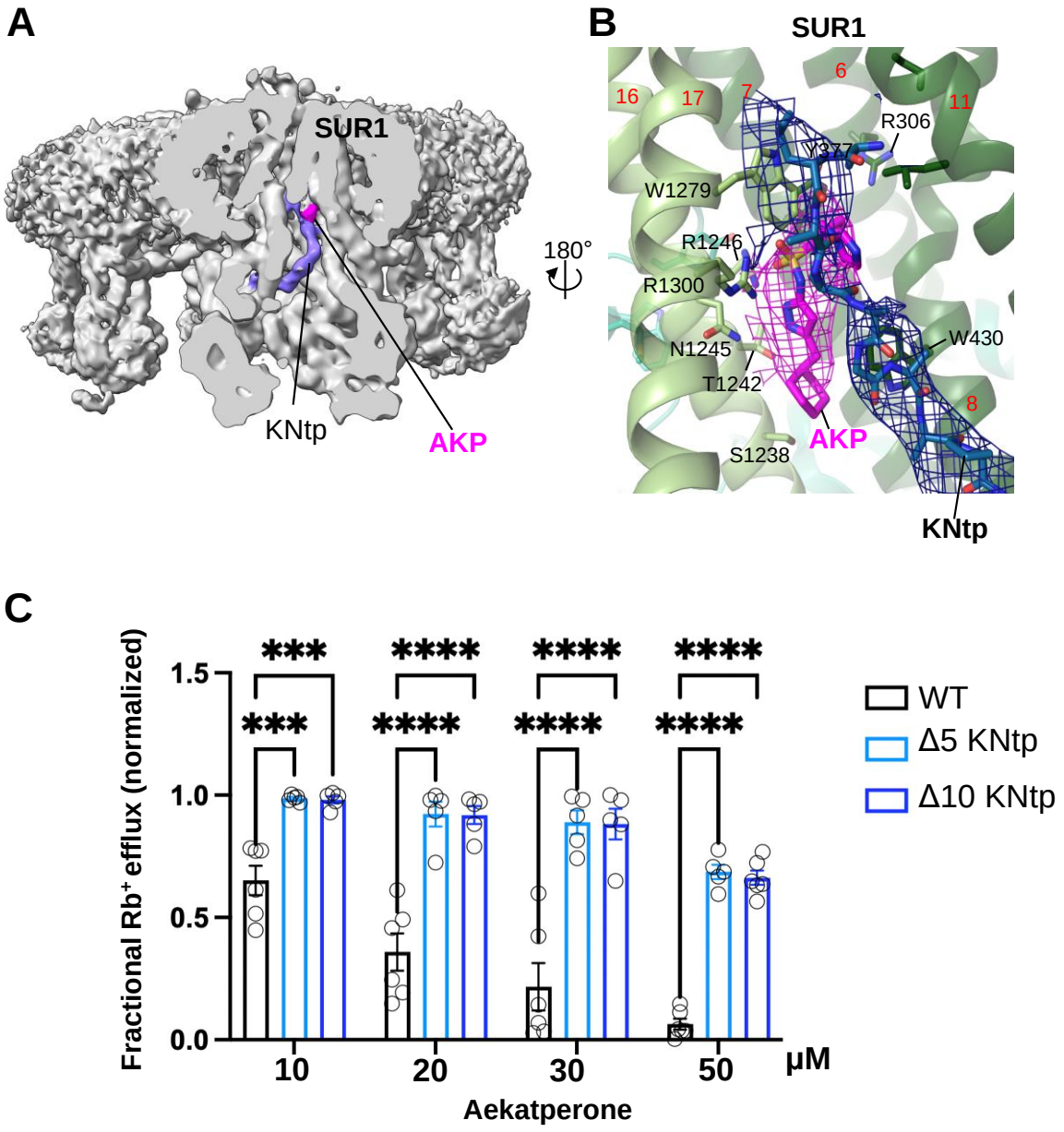

Figure 8. KNtp plays a role in Aekatperone-induced inhibitory effects on pancreatic K_{ATP} channel. (A) CryoEM density map of the pancreatic K_{ATP} channel in complex with Aekatperone (AKP), with the SUR1 subunit in the front shown in vertical sliced view. KNtp is highlighted in blue and Aekaperone in magenta. **(B)** Close-up view of the AKP (magenta) and KNtp (blue) structures overlayed with corresponding cryoEM densities (at 0.08 V) showing the close proximity of the imidazole group of Aekatperone to KNtp. **(C)** Comparison of the effects of Aekatperone on COSm6 cells expressing either WT K_{ATP} channels or channels with KNtp deletions of either 5 or 10 amino acids (Δ5 or Δ10 KNtp) using the Rb^+ efflux assay. Rb^+ efflux assays were performed in the presence of metabolic inhibitors with various concentrations of Aekatperone as indicated on the x-axis. The data were normalized against the fractional Rb^+ efflux of untreated cells expressing either WT or KNtp mutant channels with metabolic inhibition but without Aekatperone. Each bar is the mean and error bars represent the SEM of 5-6 independent experiments (individual data points shown as light black circles). Statistical significance is based on two-way ANOVA and Tukey's *post-hoc* multiple comparisons test. Alpha = 0.05. $^{**}p < 0.01$, $^{***}p < 0.001$, $^{****}p < 0.0001$.

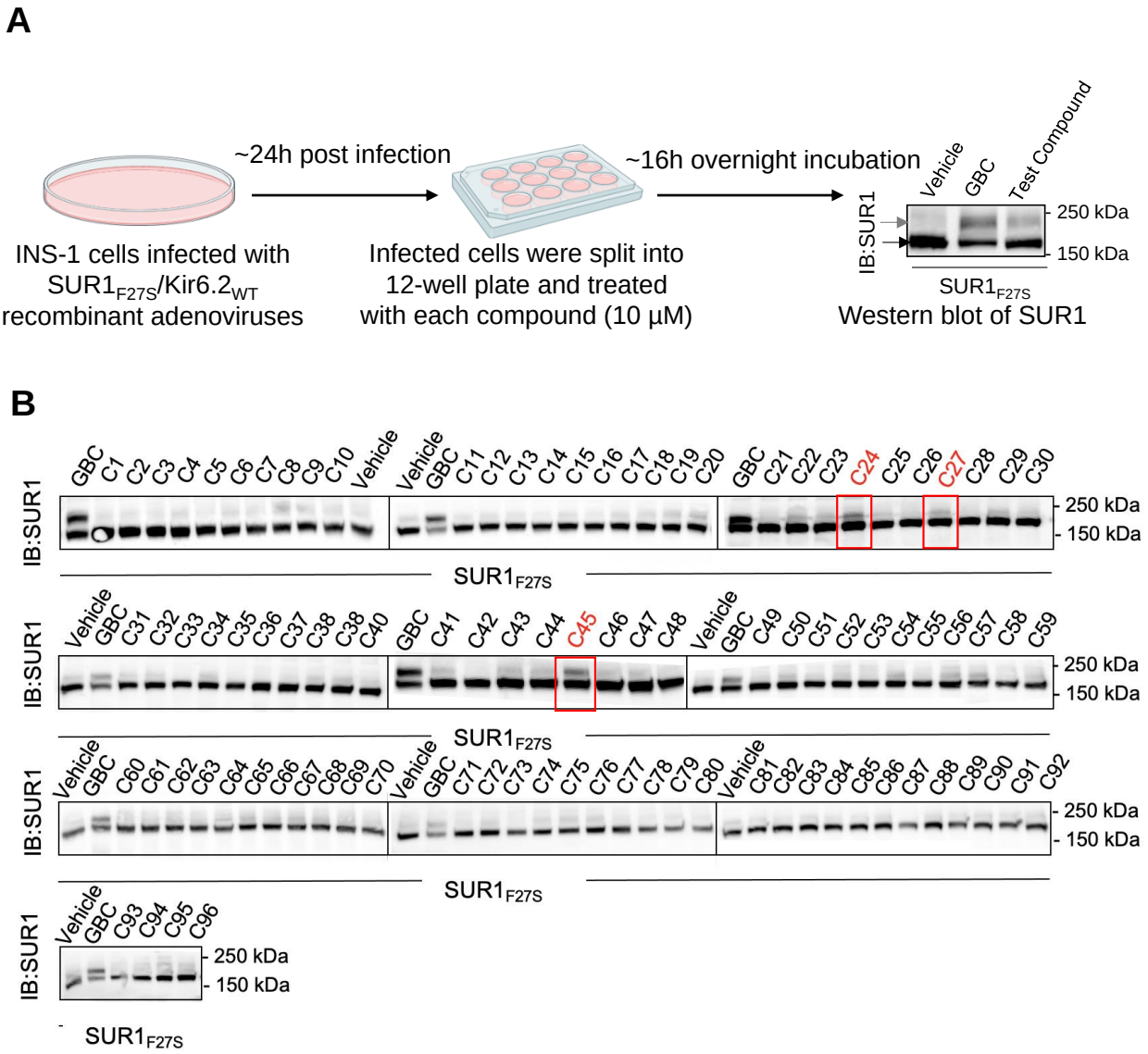

Supplementary Figure 1. Experimental testing of the top 96 compounds identified from AtomNet-based virtual screening. (A) Experimental workflow to screen for potential pharmacochaperone effects of the top scoring 96 compounds from virtual screening **(**see **Supplementary Table 1**). INS-1 cells co-expressing the trafficking mutant $SUR1_{F27S}$ and Kir6.2 WT were treated with 10 µM of one of the 96 compounds for 16 hours and harvested for western blot of SUR1. Cells treated with 0.1% DMSO served as a vehicle control, while cells treated with 10 µM glibenclamide (GBC) was used as a positive control. The lower band (black arrow) corresponds to the core-glycosylated immature SUR1, and the upper band (gray arrow) the complex-glycosylated mature SUR1. Molecular mass markers in kilodaltons (kDa) are shown on the right of the blots. **(B)** Western blots showing the effects of the 96 compounds tested, with the top three compounds (C24, C27, and C45) highlighted by red boxes. Experiments were conducted twice with similar results.

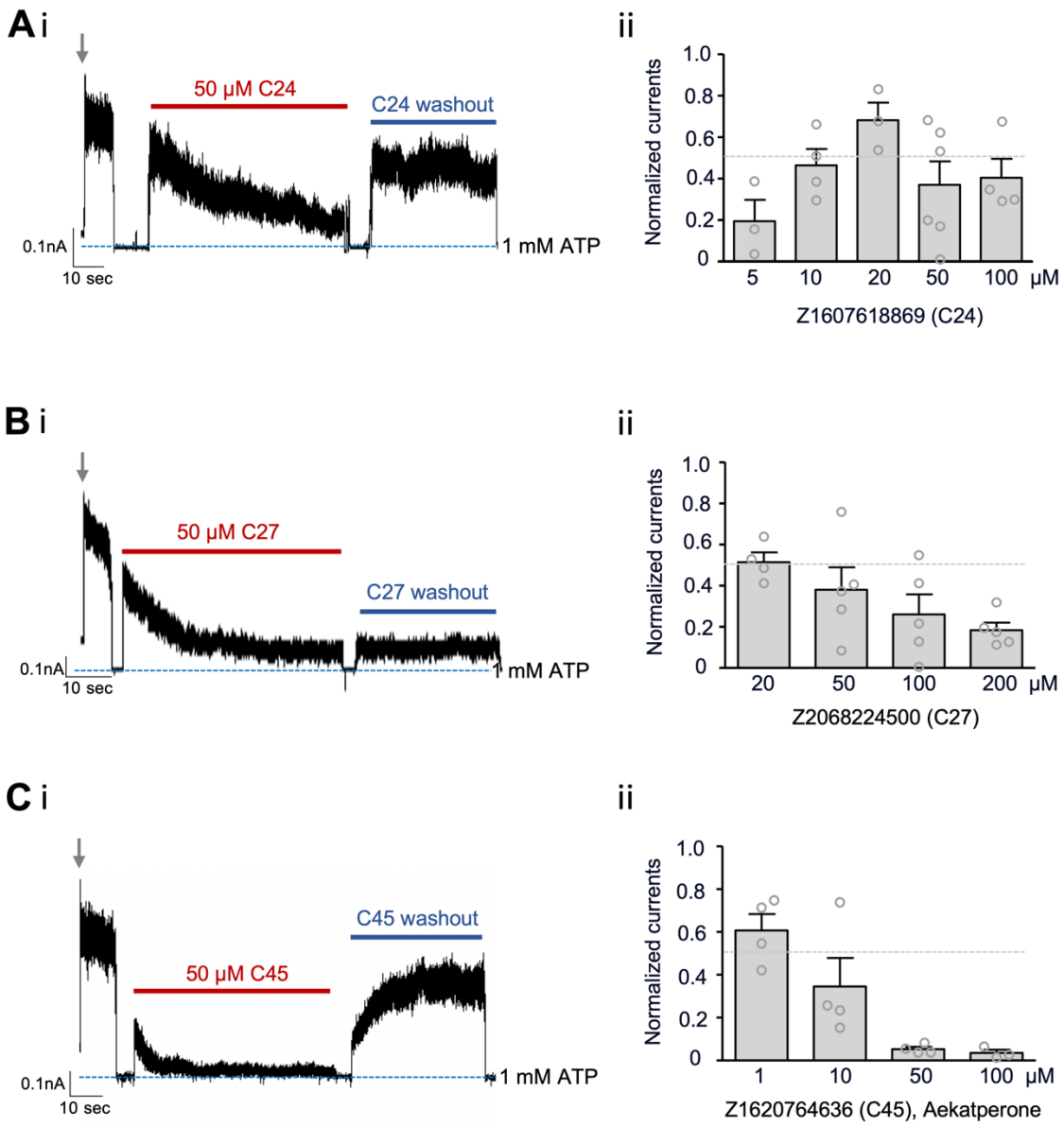

Supplementary Figure 2. The top three compounds identified via western blot screening assay inhibit K_{ATP} channel activity. (Ai, Bi, Ci) Representative inside-out patch-clamp recordings of COSm6 cells expressing WT SUR1/Kir6.2 channels. Patches were excised into K-INT/1 mM EDTA solution (indicated by the grey arrows), and then exposed to the same solution containing 50 μM of C24 (A), C27 (B), or C45 (C), followed by washout of the compounds to assess reversibility. Patches were exposed to K-INT/1 mM EDTA plus 1 mM ATP in between solution exchanges to monitor baseline (blue dashed line). Recordings were conducted at -50 mV and inward currents displayed as upward deflections. The vertical scale bar indicates current amplitudes in nanoamperes (nA), and the horizontal scale bar represents recording duration in seconds. **(Aii, Bii, Cii)** Steady-state inhibition by C24 (A), C27 (B), and C45 (C) at various concentrations indicated in the x-axis. Currents in the presence of the compounds at steady state (the end of compound exposure) were normalized to currents seen in K-INT/1 mM EDTA at the time of patch excision. Each bar represents the mean ± SEM of 3-6 patches (grey circles). The dotted grey line marks 50% inhibition.

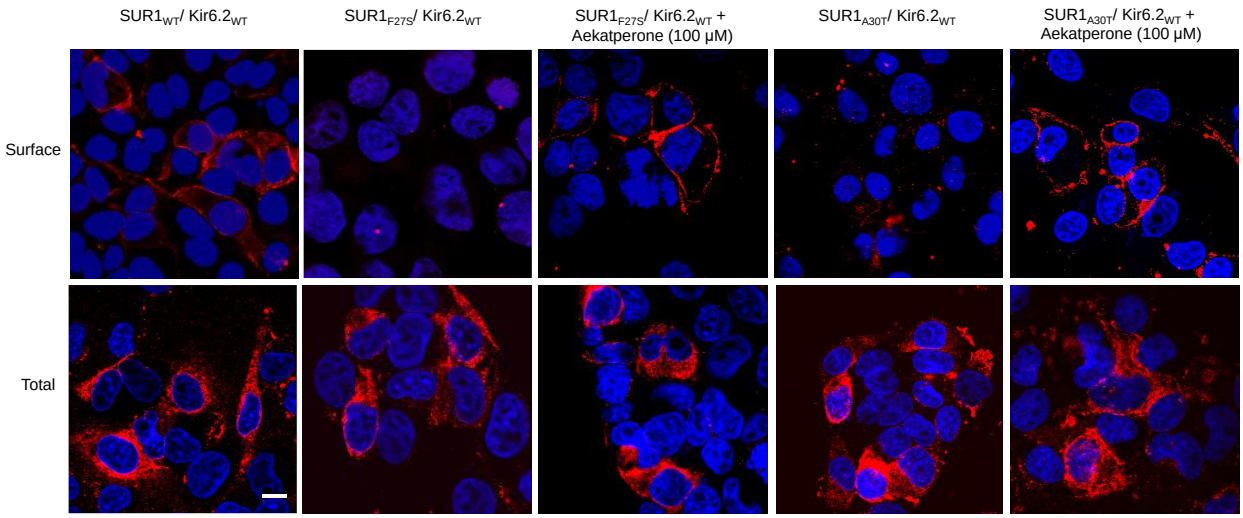

Supplementary Figure 3. Aekatperone rescues surface expression of SUR1F27S and SUR1A30T trafficking mutants. ***Top*****:** Surface staining of COSm6 cells transiently co-transfected with Kir6.2WT and various FLAG-tagged (extracellular N-terminus) SUR1 constructs (WT, F27S, or A30T) treated with or without Aekatperone using M2 anti-FLAG mouse monoclonal antibody followed by Alexa Fluor™ 546-conjugated anti-mouse secondary antibody. ***Bottom*****:** Total cellular staining of FLAG-tagged SUR1. Cells were fixed and permeabilized prior to incubation with primary and secondary antibodies. Images shown are stacked Olympic Fluoview confocal sections, with nuclei counterstained using DAPI. *Scale bar*, 10 µm.

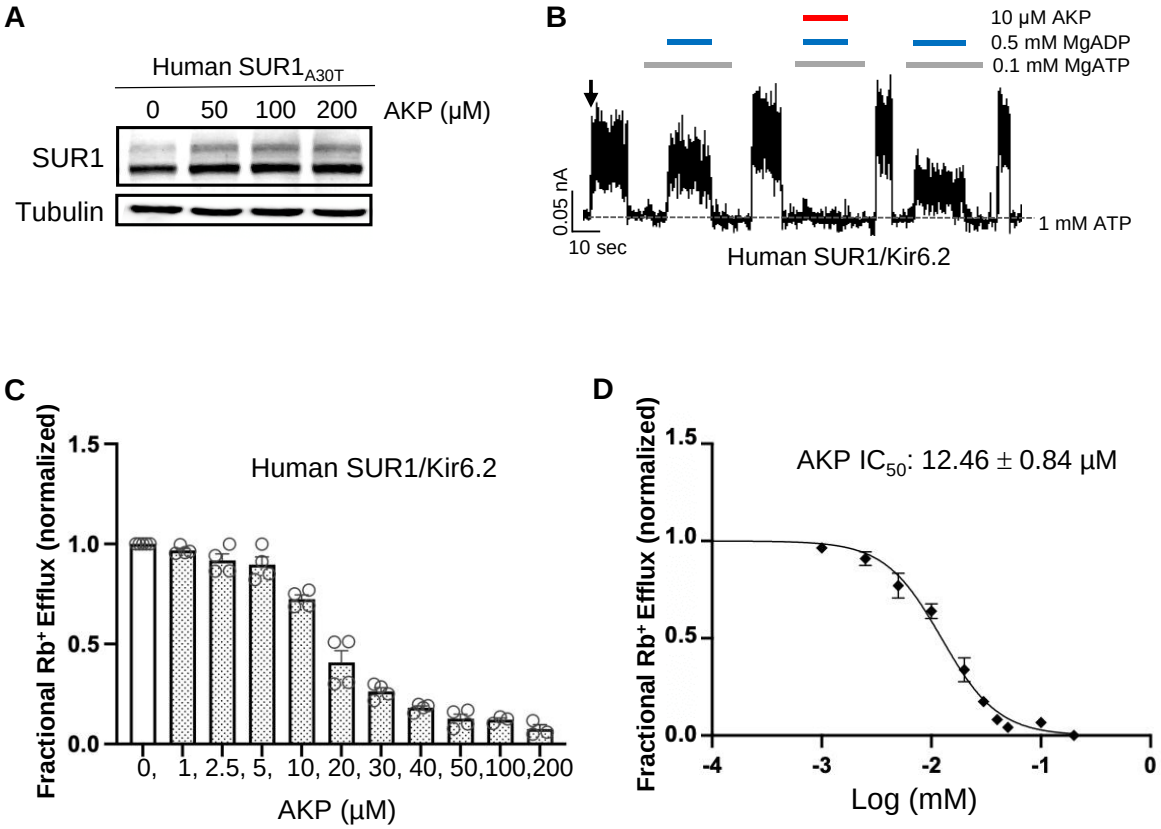

Supplementary Figure 4. Aekatperone has the same pharmacochaperoning and inhibitory effects on human K_{ATP} channels. (A) Representative western blot of SUR1 from COSm6 cells co-transfected with cDNAs of WT human Kir6.2 and human $SUR1_{A30T}$ trafficking mutant, and treated with either 0.1 % DMSO (0 μM) or various concentrations of Aekatperone (AKP) for 16 hours. **(B)** Representative recording from COSm6 cells co-transfected with human SUR1 and Kir6.2. Channels were exposed to K-INT solution upon patch excision (arrow) and exposed to solutions containing MgATP, MgADP, or Aekatperone as indicated by the bars above the recordings and the labels on the right. The patch was exposed to 1 mM ATP periodically to ensure the baseline has not shifted (grey dashed line). **(C)** Rb^+ efflux assay results showing Aekatperone dose-dependently inhibits human WT K_{ATP} channels expressed in COSm6 cells and opened by metabolic inhibition (see Methods). The fractional Rb^+ efflux was calculated by subtracting efflux in untransfected cells and normalizing to efflux in cells treated with 0.1% DMSO. **(D)** Aekatperone inhibition dose-response curve from data shown in (C) fitted with a Hill equation with variable slope using GraphPad Prism 10.

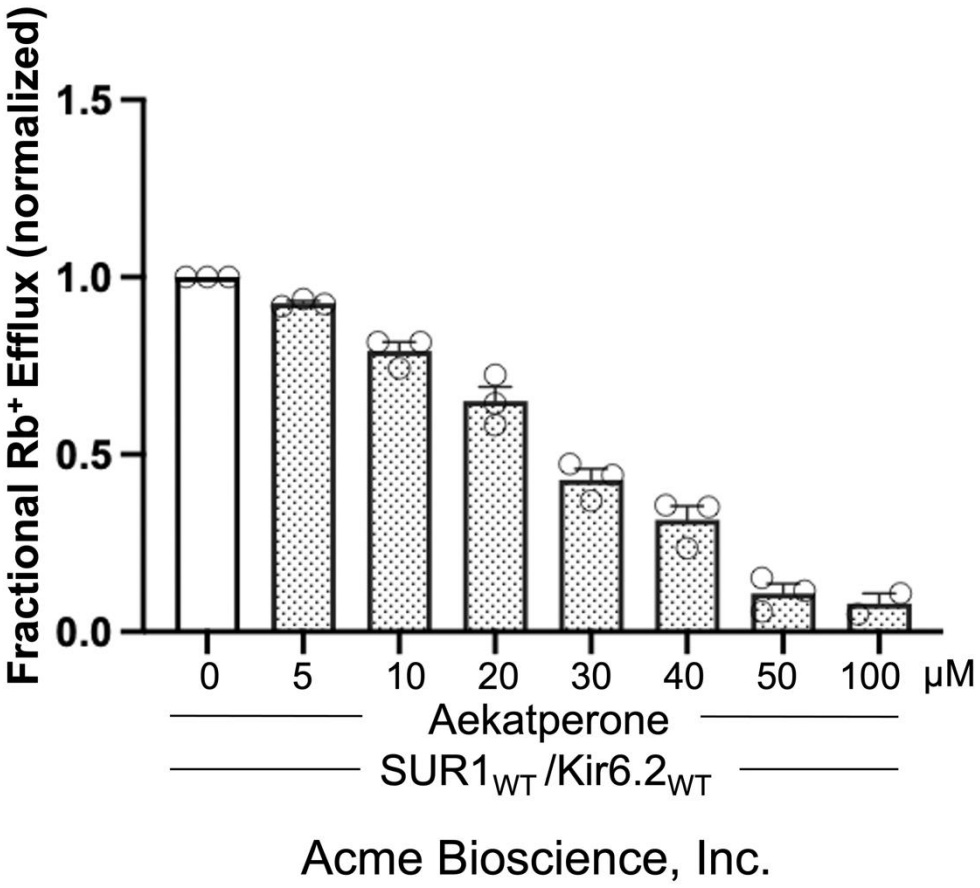

Supplementary Figure 5. Acute inhibitory effect of Aekatperone purchased from Acme Bioscience, Inc. Note the exact concentrations of Aekatperone may not precisely match those shown in Figure 3A due to the very small quantity received from Acme Bioscience, which made reconstitution less accurate.

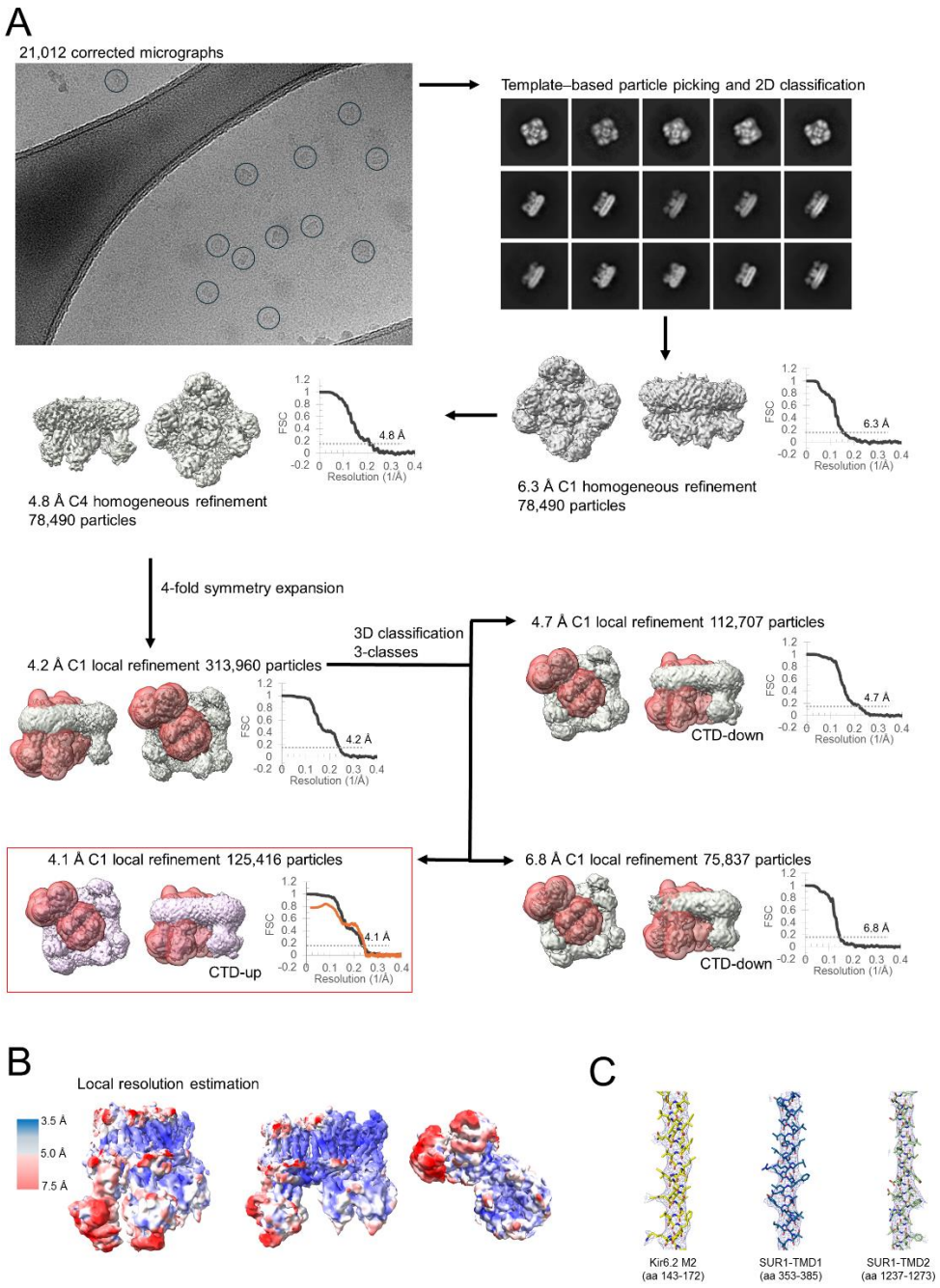

Supplementary Figure 6. CryoEM data processing. (A) Workflow showing the total number of particles yielding the 4.1 Å C1 non-uniform refinement reconstruction is 125,416. The raw image on the top left corner serve to illustrate the particles on GO layer (GO edges are seen in the left micrograph) selected (grey circles) for processing. The Fourier Shell Correlation (FSC) curve between two independent half-maps calculated for each refinement is located near the map. Where masks are applied, the mask used for its FSC calculations is shown in red. For the final map (red box), both Fourier Shell Correlation (FSC) curve between two independent half-maps (red curve) and between model and map (unmasked; PDB ID 9DFX and EMD-46820). For GSFSC calculations, FSC automask was applied. FSC curves were calculated in Phenix and cryoSPARC. **(B)** Local resolution estimate for the reconstructed map at 0.08 V contour, with micelle density not shown, in side view (left, middle) and down-top view (right). No local filtering or local sharpening was used for visualization. Local resolution estimates were calculated in cryoSPARC and visualized in ChimeraX. **(C)** Representative close-up views of cryoEM density map (blue mesh, at 0.08 V contour) superposed with the structural model.

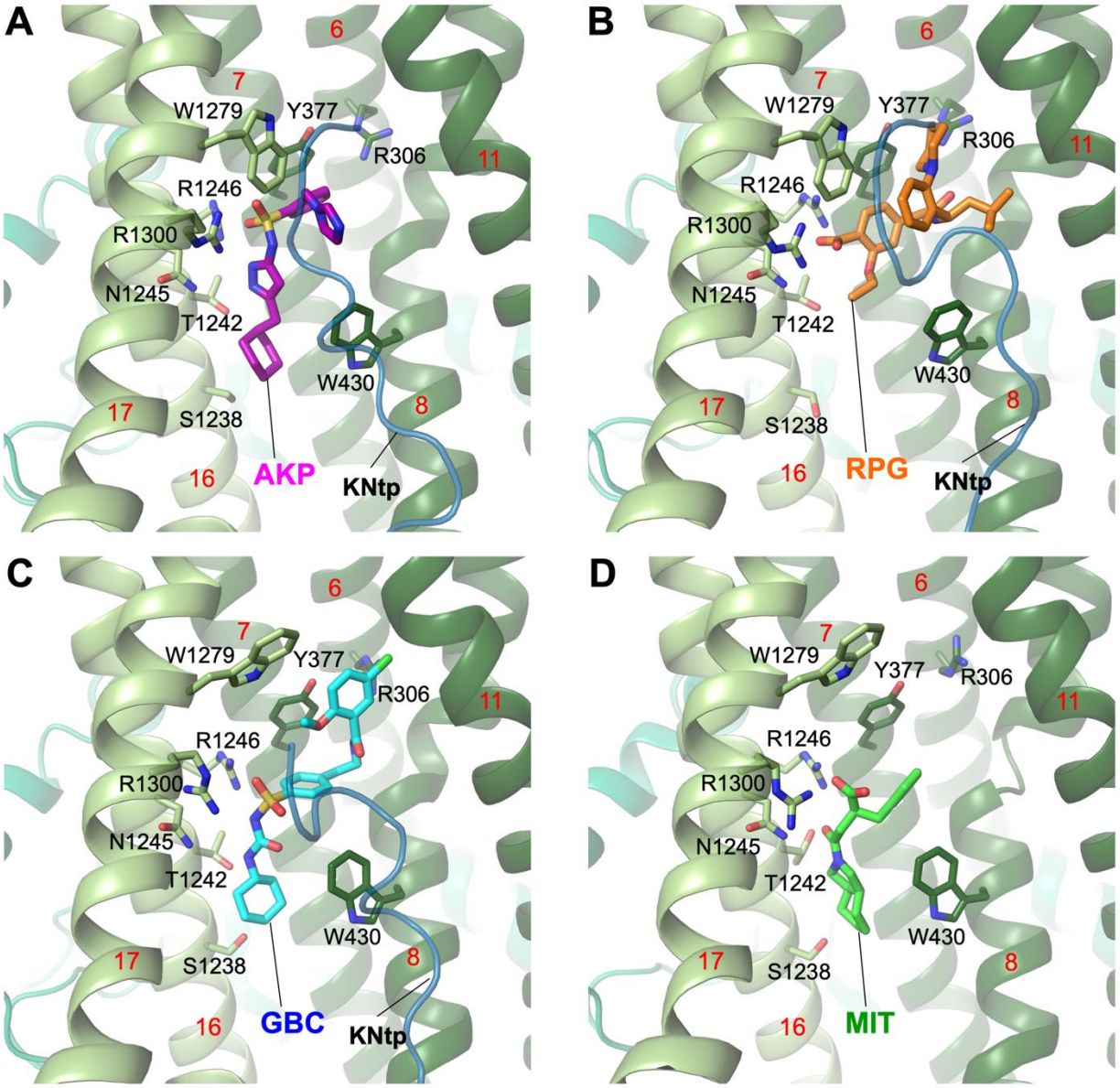

Supplementary Figure 7. Binding site model for **(A)** Aekatperone (AKP), **(B)** Repaglinide (RPG, PDB ID 7TYS), **(C)** Glibenclamide (GBC, PDB ID 7U24) bound to pancreatic K_{ATP} channels, and **(D)** Mitiglinide (MIT, PDB ID 7WIT) bound to a truncated SUR1 missing amino acids 2-208 in the absence of the Kir6.2 subunit. In A-C, KNtp is shown as a blue peptide backbone.

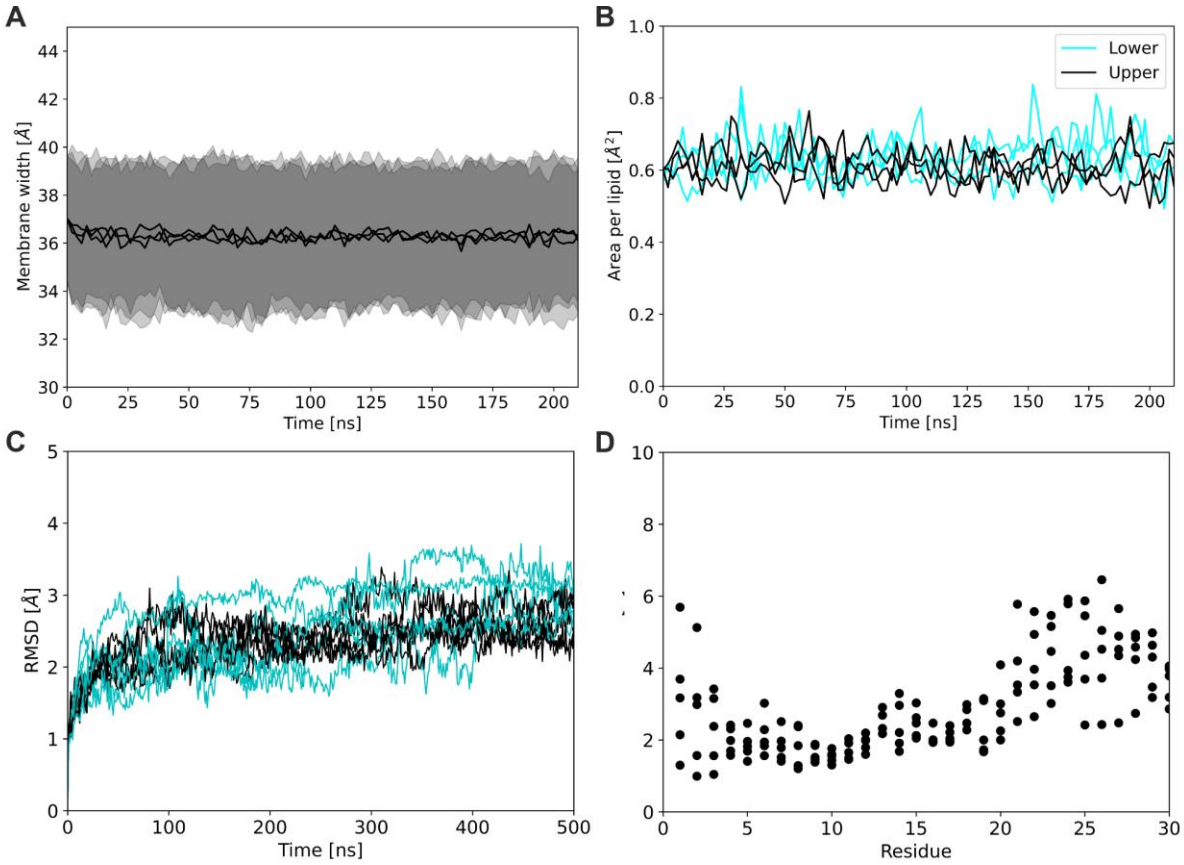

Supplementary Figure 8. Properties of the system during the extended equilibration of the system (200 ns). Calculated fluctuations in membrane thickness **(A)** and area per lipid indicating membrane density (black and cyan colors correspond to the upper and lower leaflet of the membrane, respectively) **(B)** suggest sufficient equilibration of the system with regard to the membrane. An additional 500 ns of simulation (5 repetitions) and the calculated RMSD values for the Kir6.2 tetramer and SUR1 protein (**C**, black and cyan respectively) indicate fairly good conformational stability of our system. Root mean square fluctuations for the N-terminal residues of Kir6.2 (**D)** located in the SUR1 pocket adjacent to the docked Aekatperone show that the first three amino acids of KNtp buried in the SUR1 pocket retained some conformational freedom and freely sampled the available space.

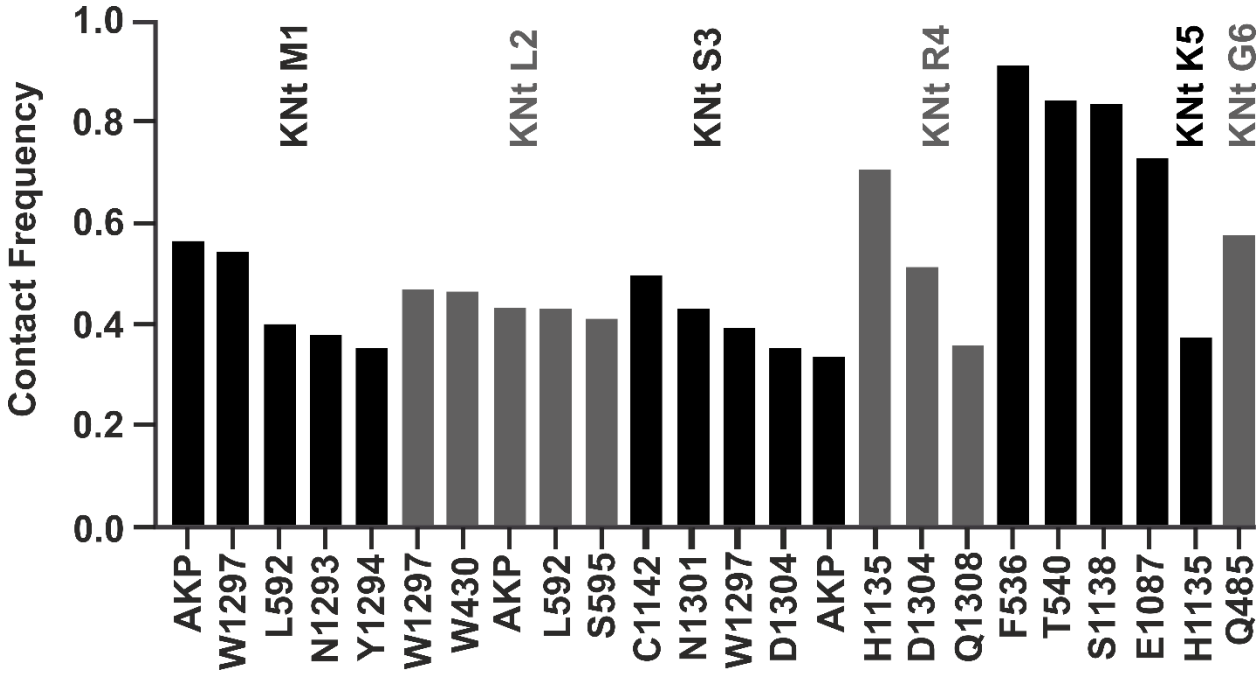

Supplementary Figure 9. Close contact frequency between first six residues of KNtp (labeled as KNt followed by residue number) and its surroundings in the Aekatperone (AKP) binding pocket.

Supplementary Table 1. Compounds from virtual screening tested using biochemical and/or functional assays (note the order of compound in the list does not correspond to the order of ranking from the virtual screening)

Compound (C) Number	ID	Formula	MW	Smile
C1	Z278092326	C22H26N2O3S	398.518	CC=1C(C)=C(C)C(=C(C)C1C)S(=O)(=O)N(CC2=CC=CO2)CC=3C=CC=NC3
C2	Z112630850	C20H19N5O2S	393.462	CC(SC1=NNC(=O)N1CC=2C=CC=CC2)C3=NN=C(O3)C=4C=CC=C(C)C4
C3	Z92024344	C22H18N4O3	386.403	OC(C(=O)OCC1=NN=NN1C=2C=CC=CC2)(C=3C=CC=CC3)C=4C=CC=CC4
C4	Z595640450	C22H22N2O4	378.421	O=C(NCC1CC=2C=CC=CC2O1)NC=3C=CC=C(COCC4=CC=CO4)C3
C5	Z299683904	C19H15N3O2S	349.406	O=S(=O)(NC=1C=CC=C2C=NNC12)C=3C=CC=CC3C=4C=CC=CC4
C6	Z1066092860	C19H19N3O3S	369.437	COC=1C=CC=CC1S(=O)(=O)NC2=C3CCCC3=NN2C=4C=CC=CC4
C7	Z1686879312	C15H21N5O2S	335.424	CC(C)C=1C=C(NS(=O)(=O)CCC2CC2)N(N1)C=3N=CC=CN3
C8	Z1643193385	C18H20N2O2S	328.428	OC1(CNC(=O)N(C=2C=CC=CC2)C=3C=CC=CC3)CCSC1
C9	Z1675091485	C17H14N2O3S	326.369	CC(=O)C1=CSC(=C1)C(=O)NC=2C(C)=NOC2C=3C=CC=CC3
C10	Z1731682842	C21H19N3O2	345.394	OC1CC=2C=CC=CC2C1NC(=O)NC=3C=CC=CC3C=4C=CN=CC4
C11	Z1833488549	C15H12Cl2N4O2S	383.252	ClC=1C=CC=C(Cl)C1CS(=O)(=O)NC2=CNN=C2C=3C=CC=CN3
C12	Z1542063934	C17H15F3N4O2S	396.386	CC=1C=C(NS(=O)(=O)CC=2C=CC=CC2)N(N1)C=3C=CC(=CN3)C(F)(F)F
C13	Z1138487193	C19H16N4O2	332.355	O=C(OCCC1=CNC=2C=CC=CC12)C=3C=NN(N3)C=4C=CC=CC4
C14	Z1838052631	C21H23N3O3	365.425	CC(NC(=O)NCC=1C=CC(=CC1)C2CC2)C=3C=CC=4OCC(=O)NC4C3
C15	Z1160819972	C16H16ClN5O2	345.783	OC(COCC=1C=CC(Cl)=CC1)CN2N=NN=C2C=3C=CC=CN3
C16	Z1955643944	C20H23N3O3S	385.479	CN1N=CC=C1C=2C=CC=CC2OCCN(CC=3C=CC=CC3)S(=O)(=O)C
C17	Z1393172784	C19H15ClN4O2S	398.866	ClC=1C=CC(=C2C=CC=CC12)S(=O)(=O)NC3=NN=CN3CC=4C=CC=CC4

C18	Z56788102	C20H16N2O2	316.353	O=C(NC=1C=CC=CC1NC(=O)C=2C=CC=CC2)C=3C=CC=CC3
C19	Z997821168	C20H17N3O3S	379.432	CN(C=1C=CC=CC1OC=2C=CC=CC2)S(=O)(=O)C3=CNC=4N=CC=CC34
C20	Z1101903992	C19H14F2N2O2	340.323	CC1=CC=C(C(=O)NC=2C=CC(F)=CC2C=3C=CC(F)=CC3)C(=O)N1
C21	Z425545360	C18H21N5O2S	371.456	CC=1C(C)=C(C)C(=C(C)C1C)S(=O)(=O)NC=2C=CC=CC2N3C=NN=N3
C22	Z806302862	C20H19N3O3	349.383	CC=1C=C(C=CC1N2CCNC2=O)C(=O)NCC3=CC=4C=CC=CC4O3
C23	Z1127155602	C21H20FN3O	349.401	CN(CC=1C=CC(=CC1)C(=O)N)C(C=2C=CC(F)=CC2)C=3C=CC=NC3
C24	Z1607618869	C23H24N4O2	388.462	CN1C(=O)CCC=2C=C(NC(=O)C=3C=C(C)N(N3)C=4C=C(C)C=C(C)C4)C=CC12
C25	Z1781382199	C15H12N2OS2	300.398	CC1=CC(=CS1)C=2N=CC=CC2NC(=O)C3=CC=CS3
C26	Z2234686034	C20H19N5O2S	393.462	CN(C)C=1C=CC=C2C(=CC=CC12)S(=O)(=O)NC=3C=CC=CC3C4=NN=CN4
C27	Z2068224500	C17H17N3O3S	343.400	O=S(=O)(NC=1C=CC=CC1C2=NC=C3CCCCN23)C=4C=COC4
C28	Z1997320230	C21H21N3O2	347.410	CC(NCC=1C=CC(NC(=O)C=2C=CC=NC2)=CC1)C=3C=CC=C(O)C3
C29	Z434838868	C21H19N3O3	361.393	COC=1C=CC(OC=2N=CC=CC2NC(=O)N3CCC=4C=CC=CC34)=CC1
C30	Z1317925131	C23H23N3O2	373.447	COC=1C=CC(CN(C)CC2=C(N=C3C=CC=CN23)C=4C=CC=CC4)=CC1O
C31	Z1332832275	C18H16N2O2S	324.396	CC=1C=CC(=CC1)C=2C=CSC2C(=O)NC=3C=NC(O)=CC3C
C32	Z1065893590	C16H15ClN4O3S	378.833	CC1=NN(C)C(OC=2C=CC=NC2)=C1NS(=O)(=O)C=3C=CC=CC3Cl
C33	Z1430522786	C15H17F2N5O2S	369.389	CC(C)N1N=CC=2C=C(C=CC12)S(=O)(=O)NC=3C=NN(CC(F)F)C3
C34	Z751820632	C16H14N2O2S3	362.489	O=S(=O)(N1CCC=2SC=CC2C1C3=CC=CS3)C=4C=CC=NC4
C35	Z857281148	C21H22N4O3	378.424	CC=1C=CC=C(C)C1N2N=NN=C2COC(=O)C=3C=C4CCCCC4=CC3O
C36	Z285781140	C18H20N4OS	340.442	CCC1=CC=2C(=NC=NC2S1)N3CCN(CC3)C=4C=CC(O)=CC4
C37	Z361864720	C18H17N3O2S	339.411	O=S(=O)(N(CC=1C=CC=C2C=CC=NC12)C3CC3)C=4C=CC=NC4

C38	Z1450943637	C16H16N4O2S2	360.453	CN1C=C(C=N1)S(=O)(=O)NC=2SC(=NC2C=3C=CC=CC3)C4CC4
C39	Z1833450474	C19H21N5O2S	383.467	CN1CCCC=2C=CC(=CC12)S(=O)(=O)NC3=CN(CC=4C=CC=CC4)N=N3
C40	Z1878392989	C18H22N4O3	342.392	O=C1CCCC=2C(OCC3=NN=NN3CC4CCOCC4)=CC=CC12
C41	Z1187995755	C19H19FN2O3	342.364	CC(NC1CCOC1=O)C=2C=CC(NC(=O)C=3C=CC(F)=CC3)=CC2
C42	Z239150122	C23H18N2O4	386.400	O=C(NC=1C=CC=C(OC=2C=CC=CC2)C1)C3=CC=C(CN4C=CC=CC4=O)O3
C43	Z184527044	C21H25N3O2	351.442	CC(=O)NC=1C=CC(NC(=O)C=2C=CC(CN3CCCCC3)=CC2)=CC1
C44	Z955248736	C20H20N2O4	352.383	O=C(NC=1C=CC=CC1C(=O)N2CCOCC2)C=3C=CC=4COCC4C3
C45	Z1620764636	C20H25N5O2S	399.509	O=S(=O)(NC1=CC(CC2CCCCC2)=NN1)C=3C=CC=CC3CN4C=CN=C4
C46	Z827062904	C13H10F3N5OS	341.311	CC(=O)C=1C=CC=CC1NC2=NN3C(=NN=C3SC2)C(F)(F)F
C47	Z19653453	C14H9N3OS3	331.435	O=C1NC(CSC2=NC=3C=CC=CC3S2)=NC=4C=CSC14
C48	Z1819546701	C21H20N6O2	388.422	CC(OC(=O)C1=CN(N=C1C=2C=CC=CC2C)C=3C=CC=CC3)C4=NN=NN4C
C49	Z1836331215	C21H23N3O3S	397.490	CN1C=C(CNS(=O)(=O)CCC=2C=CC=3OCCC3C2)C(=N1)C=4C=CC=CC4
C50	Z1071096112	C16H17BrN2O2	349.222	COC=1C=CC(Br)=C(CNCC=2C=CC=C(C2)C(=O)N)C1
C51	Z225706824	C14H17N3OS2	307.434	CC=1C=C(SC1C)C(=O)N2CCN(CC2)C3=NC=CS3
C52	Z202727764	C20H18ClN3O4	399.827	CC=1C=CC(OC=2C=CC(Cl)=CC2NC(=O)COC(=O)C=3C=NN(C)C3)=CC1
C53	Z229456558	C21H21N5O3	391.423	O=C(C1CCN(CC1)C2=NN=NN2C=3C=CC=CC3)C=4C=CC=5OCCOC5C4
C54	Z281793560	C22H23N3O3	377.436	CN(C)C(CNC(=O)C=1C=CC(NC(=O)C=2C=CC=CC2)=CC1)C3=CC=CO3
C55	Z199879632	C21H21N3O3S	395.474	CCOC(=O)C=1C=CSC1NC(=O)CNC(C=2C=CC=CC2)C=3C=CC=CN3
C56	Z118712240	C20H22N2O4	354.399	CCN1C=C(C(=O)NC=2C=C(OC)C(OC)=C(OC)C2)C=3C=CC=CC13
C57	Z53195724	C21H19N5O2	373.407	O=C1CCCC2=C1C(C=3C=CC=CC3OCC=4C=CC=CC4)N5N=NN=C5N2

C58	Z229339834	C19H24N6O2	368.432	COC=1C=C(CCC2CCN(CC2)C=3C=CC4=NN=NN4N3)C=C(OC)C1
C59	Z108853906	C23H21N5O	383.445	O=C(NC(C=1C=CC=CC1)C=2C=CC=CC2)C(CC=3C=CC=CC3)N4C=NN=N4
C60	Z195664472	C21H23N3O3	365.425	COC=1C=CC(CCNC(C(=O)NC=2C=C(C)ON2)C=3C=CC=CC3)=CC1
C61	Z27654017	C22H20N2O2	344.406	CC(=O)NC=1C=CC(NC(=O)C(C=2C=CC=CC2)C=3C=CC=CC3)=CC1
C62	Z18520264	C14H24N4O2S	312.430	CC(C)C1CCC(C)CC1OC(=O)CSC2=NN=NN2C
C63	Z432733912	C19H17N3O	303.357	O=C(NC=1C=CC=C2C=NC=CC12)N3CCC3C=4C=CC=CC4
C64	Z736530444	C16H14ClN3O2S	347.819	ClC=1N=C2C=CC=CN2C1S(=O)(=O)NC3CCC=4C=CC=CC34
C65	Z971175648	C13H13N5O2S	303.339	CC1=CC=NN1C=2C=CC=C(NS(=O)(=O)C=3C=NNC3)C2
C66	Z650466608	C22H21N3O2	359.421	O=C(CCC=1C=CN=CC1)NCC=2C=CC=C(C2)C(=O)NC=3C=CC=CC3
C67	Z435060562	C20H23N3O4	369.414	CC(C)C(=O)NC=1C=CC(C)=C(NC(=O)NCC=2C=CC=3OCOC3C2)C1
C68	Z643123666	C20H23N3O4	369.414	COC(=O)C=1C=CC(NCC2(CCCC2)C=3C=CC=4OCCOC4C3)=NN1
C69	Z454392778	C20H18N2O3S2	398.498	CNS(=O)(=O)C=1C=CC(C2=CC=CS2)=C(C1)C(=O)N3CCC=4C=CC=CC34
C70	Z729771054	C23H24ClN3O	393.909	Cl.COC=1C=CC=2C=CC=CC2C1CNCC=3C=CC=CC3CN4C=CN=C4
C71	Z194689474	C15H12N4OS3	360.476	C(CSC=1N=CN=C2C=CSC12)CC3=NC(=NO3)C4=CC=CS4
C72	Z744593102	C13H10INO3S	387.192	CC=1C=C(NC(=O)C=2C=CC=CC2I)SC1C(=O)O
C73	Z19674372	C19H16N2O4S	368.406	CC(OC(=O)C=1C=CC(O)=CC1)C(=O)NC2=NC(=CS2)C=3C=CC=CC3
C74	Z278198642	C20H24N4O3	368.429	CC(C)(C)C=1C=CC(OCC(O)CN2N=NN(C=3C=CC=CC3)C2=O)=CC1
C75	Z114094422	C19H15N3O3	333.340	O=C(OCCOC=1C=CC(C#N)=CC1)C=2C=C(NN2)C=3C=CC=CC3
C76	Z70997953	C24H19N3O3	397.425	CC=1C=CC2=NC(=C(NC(=O)C3CC=4C=CC=CC4C(=O)O3)N2C1)C=5C=CC=CC5
C77	Z244248008	C23H21N3O3	387.431	CC1=CC=CN2C=C(COC=3C=CC=CC3C(=O)NOCC=4C=CC=CC4)N=C12

C78	Z117598840	C22H23N3O2S	393.501	CN(C)CC(NC(=O)C=1C=CC=C(NC(=O)C2=CC=CS2)C1)C=3C=CC=CC3
C79	Z195760046	C18H22N2O	282.380	CCCC(NCC=1C=CC(=CC1)C(=O)N)C=2C=CC=CC2
C80	Z25939025	C23H22N4O2	386.446	O=C(CON1N=NC=2C=CC=CC12)NCCC(C=3C=CC=CC3)C=4C=CC=CC4
C81	Z52058186	C21H19N3O2S	377.459	CC1=NC(=CS1)C=2C=CC=C(NC(=O)C=3C=CC(=CC3)N4CCCC4=O)C2
C82	Z199510658	C17H21NO4S	335.417	CCOC=1C=CC(=CC1S(=O)(=O)NC=2C=CC=CC2O)C(C)C
C83	Z57705742	C24H23NO3	373.444	O=C(CN(CC=1C=CC=CC1)CC=2C=CC=CC2)OCC(=O)C=3C=CC=CC3
C84	Z55868904	C19H19N3O2S	353.438	CC=1SC=2N(CN(CC=3C=CC=NC3)CC2C1C)C(=O)C4=CC=CO4
C85	Z25397974	C16H15N3OS2	329.439	O=C(CCCSC1=NN=C(N1)C=2C=CC=CC2)C3=CC=CS3
C86	Z218663160	C20H16N4O2S	376.431	NC(=O)C(SC1=NN=C(C2=CC=CO2)N1C=3C=CC=CC3)C=4C=CC=CC4
C87	Z106784726	C22H23N5S	389.516	CC(C)C=1C=CC(=CC1)C(NCC2=NN=NN2C=3C=CC=CC3)C4=CC=CS4
C88	Z88331415	C18H14N2O2S	322.380	CC(=O)C1=CC=C(S1)C=2C=CC=CC2NC(=O)C=3C=CC=CN3
C89	Z135439958	C21H21N3O3	363.409	CCN(CC)C(=O)C=1C=CC=C(NC(=O)C2=CC(=O)NC=3C=CC=CC23)C1
C90	Z85917655	C19H18N4O2S	366.436	CC1=C(C(C2=CC=C(C)S2)N3N=CN=C3N1)C(=O)OCC=4C=CC=CC4
C91	Z19883124	C20H19N3O3S	381.448	COC=1C=CC(=CC1)N2C(SC3CCOC3=O)=NN=C2C=4C=CC=C(C)C4
C92	Z27798110	C19H18N2O2	306.358	CC=1ON=C(C1C(=O)NC=2C=CC=C(C)C2C)C=3C=CC=CC3
C93	Z185185866	C19H21N3O2S	355.453	CC=1C=CC(C)=C(C1)S(=O)(=O)NC(C2=NC=CN2C)C=3C=CC=CC3
C94	Z57003550	C18H16N2O4S	356.395	OC(=O)CCC1=CC=C(C2=CC=CS2)N1NC(=O)C=3C=CC(O)=CC3
C95	Z26545746	C22H17N3O2	355.389	CN1N=C(C(=O)NC=2C=CC=CC2C=3C=CC=CC3)C=4C=CC=CC4C1=O
C96	Z146826758	C22H22N4O2	374.435	CC1=NN(C(C)=C1C(=O)NC=2C=CC=C(C2)C(=O)NC3CC3)C=4C=CC=CC4

Supplementary Table 2. Model statistics of the AKP-bound SUR1/Kir6.2 structure

Data Collection	
Microscope	Titan Krios
Voltage (kV)	300
Camera	Gatan K3
Camera mode	Super-resolution
Defocus range (μm)	-1.0 ~ -2.5
Movies	21,012
Frames/movie	74
Exposure time (s)	3.2
Frame rate (/s)	23
Magnified pixel size (Å)*	1.0515
Total dose ($e^-/Å^2$)	~55
Reconstruction	
Software	Cryosparc 4.2.1
Symmetry	C4
Mask	Full K_{ATP}
Particles refined	125,416 C4 symmetry-expanded particles
Resolution (masked)	4.1 Å
Refinement Statistics	
PDB ID[1]	9DFX
EMDataResource	EMD-46820
Atoms	20552
Protein residues	2871
Map CC (masked)	0.75
FSC model (0.143, 0.5)	4.1, 5.9
Clash score	5.14
Molprobity score	1.27
Cβ deviations	0
Rotamer outliers (%)	3.45
ADP (mean protein)	287.65
ADP (mean ligands)	303.33
Ramachandran	
Outliers	0.00
Allowed	2.00
Favored	98.0
Bonds (RMSD)	
Length (Å)	0.001
Bond angles	0.382

[1]PDB ID 9DFX/EMD-46820 contains the Kir6.2 tetramer and one of four SUR1 subunits of the K_{ATP} channel
*Super-resolution pixel size 0.52575 Å